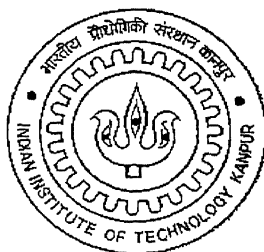


Synthesis and Characterization of $\text{Li}_2\text{SO}_4\text{-FeSO}_4$ Superionic System

A Thesis Submitted
in Partial Fulfillment of the Requirements
for the Degree of
Master of Technology

By
Gopinadhan K.



To the
Materials Science Programme
Indian Institute of Technology, Kanpur
July, 2002

3 FEB 2003 /MSP

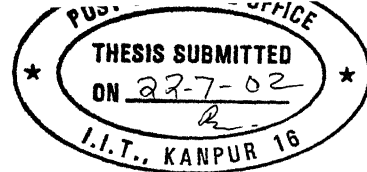
पुरुषोत्तम काशीनाथ केलकर पुस्तकालय

भारतीय प्रौद्योगिकी संस्थान कानपुर

अवधि क्र० A 141851



A141851



CERTIFICATE

It is certify that the work presented in this title entitled ‘Synthesis and Characterization of Li_2SO_4 - FeSO_4 Superionic System”, K. Gopinadhan, has been carried out under my supervision and that work has not been submitted elsewhere for a degree.

IIT Kanpur

July, 2002

(Prof. K. Shahi)

Thesis Supervisor

Materials Science Programme

IIT Kanpur

ABSTRACT

In the present work, the main motivation is to study the basic mechanisms of conductivity in lithium sulphate based electrolytes, and also to bring down the transition temperature from 584°C to a lower temperature. Lithium sulphate exhibits a well known first order phase transition near 584°C. With the aim of reducing the transition temperature, FeSO₄ is used as a dopant. Thirteen different compositions of Li₂SO₄+ x FeSO₄, with $0 \leq x \leq 1$ are synthesized and studied using different techniques. Of these mechanical mixing proved to be the best. A maximum reduction of ~ 87°C in the transition temperature is observed for the composition Li₂SO₄ + 0.40 FeSO₄. All other compositions containing $x > 0.40$, show a broad/diffuse transition over a range of temperature, rather than a sharp one. All these experiments have been repeated twice to check the validity of the data. The structural characterization is done by X-ray diffraction (XRD), BET and Fourier transform infrared spectroscopy (FT-IR). The electrical properties are studied by measuring the dc conductivity of the samples.

ACKNOWLEDGEMENT

I am deeply indebted to Prof K. Shahi who guided and inspired me, giving confidence and enthusiasm in a situation of patience and concentration. He has been a constant source of inspiration with never give up attitude. It is a nice experience to work with him. The way he made me think and work has an everlasting impact on my career. I am expressing my sincere thanks to him who helped me to make this moment a memorable one

I am grateful to my teacher Prof. Samares Kar, who constantly encouraged and inspired me, giving valuable advices and knowledge, made my student's life at IITK an everlasting and memorable one. The way he made me to think and work remains as a bright star in the sky of my student's life.

I am grateful to Mr Uma Shankar (X-ray lab), Mr. T. B. Pandey (Solid state ionics lab), Mr. Sushanta Pal (Materials testing lab, BET), Mr. S.B. Pandey, Mr. K Rajagopalan (Micro analytical lab), Mr Karthikeyan (Instrumentation lab), Mr Jai Kishan (Machine shop), Mr. B. Sharma (Teaching lab), Mr. Joshi (MSP office), Physics workshop staff Mr. Sampat Singh and Central work shop staff Mr. Srivastava for their incredible work which helped me to finish within time

I am grateful to all my labmates Anshuman, Jai Prakash, Tathagata, Mukesh and Abhishek for their cooperation, suggestions and encouragement throughout my work.

I am thankful to my friends Aditi, Anisia, Praveen, Pooja, Dulal, Rajesh, Pradeep, Unni, Bejoy, Suresh, Vishak, Manoj, Debadi. and Santanu for constantly helping me and making my stay at IITK a memorable one.

Last but not the least, from the bottom of my heart I am deeply indebted to my mother, father and sisters for their ceaseless inspiration and constant encouragement.

CONTENTS

1.INTRODUCTION	1
1.1 General Theory of Ionic Conductors	2
1.2 Classification of Ionic Solids	4
1.2.1 Nature Dependent Classification	4
1.2.2 Transition Dependent Classification	6
1.3 Importance of Solid Electrolytes	8
1.4 Maxwell Model for Composite Electrolytes	8
1.5 Importance of Lithium Based electrolytes	9
1.6 Lithium Sulphate (Li_2SO_4), a special material of interest	9
1.7 Recent Progress	13
1.8 Statement of the Problem	18
 2. EXPERIMENTAL DETAILS AND CHARACTERIZATION TECHNIQUES	 19
2.1 Experimental Details	19
2.1.1 Sample Holder	20
2.1.2 Furnace and Temperature Controller	21
2.1.3 Impedance Analyzer	21
2.1.4 Experimental Arrangement	22
2.2 Structural Analysis by X-Ray powder Diffraction (XRD)	23
2.3 BET Measurement	24

2.4 Fourier Transform Infrared Spectroscopy (FT-IR)	25
2.5 Complex Impedance Analysis	27
2.5.1 Pure Resistor Circuit	28
2.5.2 Pure Capacitor Circuit	29
2.5.3 Series Combination of R and C	30
2.5.4 Parallel Combination of R and C	31
2.6 Impedance Measurement Methodology	35
2.7 Materials Processing	36
2.8 Sample Preparation	37
 3. RESULTS AND DISCUSSION	 39
 3.1 X-Ray powder Diffraction (XRD)	 39
3.1.1 Particle Size determination	40
3.2 BET measurements	44
3.3 Fourier Transform Infrared Spectroscopy (FT-IR)	45
3.4 Impedance Analysis	49
3.5 DC conductivity	51
3.5.1 Conventional Samples	52
3.6 Maxwell Classical Model	73
 4. SUMMARY AND CONCLUSIONS	 75

LIST OF FIGURES

Figure No.	Figure caption	Page No.
1.1	Structural phase transitions of Li_2SO_4	11
1.2	Structure of $\alpha\text{-Li}_2\text{SO}_4$	12
2.1	Sample holder for complex impedance analysis	20
2.2	Block diagram of the experimental set-up used in the ionic conductivity measurements	23
2.3	Impedance plot for a purely resistive circuit	29
2.4	Impedance plot for a purely capacitive circuit	30
2.5	Impedance plot for a resistor and a capacitor in series	30
2.6(a)	Impedance plot for a resistor and a capacitor in parallel	32
2.6(b)	Effect of interface capacitance C_i on impedance of electrolyte	33
2.6(c)	Depression of semicircle	34
2.6(d)	Grain boundary effect	34
3.1	XRD patterns for the pure Li_2SO_4 and $\text{Li}_2\text{SO}_4 + 5 \text{ m/o}$ FeSO_4 samples	41
3.2	XRD patterns for the $\text{Li}_2\text{SO}_4 + 10 \text{ m/o}$ FeSO_4 and $\text{Li}_2\text{SO}_4 + 20 \text{ m/o}$ FeSO_4 samples	42
3.3	XRD patterns for the $\text{Li}_2\text{SO}_4 + 40 \text{ m/o}$ FeSO_4 and pure FeSO_4 samples	43
3.4	FT-IR spectra of pure Li_2SO_4 and $\text{Li}_2\text{SO}_4 + 20 \text{ m/o}$ FeSO_4 samples	47
3.5	FT-IR spectra of $\text{Li}_2\text{SO}_4 + 30 \text{ m/o}$ FeSO_4 and $\text{Li}_2\text{SO}_4 + 40 \text{ m/o}$ FeSO_4 samples	48

3.6(a) Impedance plot for pure Li_2SO_4 at 395, 417 and 437 °C	49
3.6(b) Impedance plot for $\text{Li}_2\text{SO}_4 + 10 \text{ m/o FeSO}_4$ at 378, 420 and 443°C	49
3.7 Impedance plot for $\text{Li}_2\text{SO}_4 + 60 \text{ m/o FeSO}_4$ at 512°C	51
3.8 DC conductivity of $\text{Li}_2\text{SO}_4 + 30 \text{ m/o FeSO}_4$ prepared by different routes	53
3.9 DC conductivity of $\text{Li}_2\text{SO}_4 + 40 \text{ m/o FeSO}_4$ prepared by different routes	54
3.10 DC conductivity of pure Li_2SO_4	55
3.11 DC conductivity of $\text{Li}_2\text{SO}_4 + 5 \text{ m/o FeSO}_4$	60
3.12 DC conductivity of $\text{Li}_2\text{SO}_4 + 10 \text{ m/o FeSO}_4$	61
3.13 DC conductivity of $\text{Li}_2\text{SO}_4 + 20 \text{ m/o FeSO}_4$	62
3.14 DC conductivity of $\text{Li}_2\text{SO}_4 + 30 \text{ m/o FeSO}_4$	63
3.15 DC conductivity of $\text{Li}_2\text{SO}_4 + 40 \text{ m/o FeSO}_4$	64
3.16 DC conductivity of $\text{Li}_2\text{SO}_4 + 50 \text{ m/o FeSO}_4$	65
3.17 DC conductivity of $\text{Li}_2\text{SO}_4 + 80 \text{ m/o FeSO}_4$	66
3.18 DC conductivity of pure FeSO_4	67
3.19 DC conductivities of all samples prepared by mechanical mixing	68
3.20 Plot of transition temperature (T_C) and knee temperature (T_N) against mole percentage of FeSO_4 in Li_2SO_4	71
3.21 Plot of dc conductivity (σ) and extrinsic energy against mole percentage of FeSO_4 in Li_2SO_4	72

LIST OF TABLES

Table No.	Table caption	Page No.
1.1	A list of materials exhibiting the various type of transitions	7
2.1	The displays 'A' and 'B' of impedance analyzer	23
2.2	The physical properties of the starting materials	36
2.3	Sintering temperature, sintering time and thickness of different samples prepared	38
3.1	Calculation of crystallite size	44
3.2	Various quantities involved in BET measurements	45
3.3	Specific surface area of two different samples	45
3.4	The observed wave numbers for SO_4^{2-} from FT-IR spectra	46
3.5	Ionic transport parameters for Li_2SO_4 - FeSO_4 system	57
3.6	Energy of migration in $\alpha\text{-Li}_2\text{SO}_4$	59
3.7	Experimental and calculated values of conductivities of $\text{Li}_2\text{SO}_4 + x \text{FeSO}_4$ system at 608 K	74

CHAPTER 1

1. Introduction

“Solid State Ionics” is a field involving the study of the phenomenon of ions in solids which exhibit high ionic conductivities at fairly low temperatures below their melting points.

Ionic conductivity was first reported by Michael Faraday [1] more than one hundred years ago. The term “Solid State Ionics” was first used in 1960 by Takahashi [2]. Solid state ionics is an interdisciplinary science, fundamental and applied, which covers physics, chemistry, and materials science involving all kinds of ionic transport in solid state. It involves ionic materials having different morphologies, which include single crystals, powder specimen, and thin films. The increasing interest in this area of research during the last few decades may be attributed to the fact that these materials are inherently leak-proof, electrochemically compatible, rugged, thermodynamically stable, and can be miniaturized for many different practical applications in electrochemical devices and power sources.

The perfect crystal would have the lowest internal energy, but a real crystal must always contain a certain number of defects in thermodynamic equilibrium. Frenkel and Schottky proposed their classical mechanisms that explain how electricity is transported through ionic solids by the flow of ions. In Frenkel disorder electricity is involved by the motion of ions from their normal lattice sites to interstitial sites (space between lattice atoms), and in Schottky mechanism, the ions move from their normal lattice sites to the surface of the crystal.

Superionic solids are materials with high electrical conductivity ($>10^{-3} \Omega^{-1}\text{cm}^{-1}$) comparable with those of liquid electrolytes. These materials are also termed solid electrolytes or fast ion conductors.

1.1 General Theory of Ionic Conductors

The electrical conductivity of any material is given by,

$$\sigma = \sum_i n_i q_i \mu_i \quad (1.1)$$

Where n_i , q_i and μ_i are the concentration, the charge and the mobility respectively of the 'i'th species. The summation is over all possible charge carriers (e.g. vacancies, interstitials, electrons and holes). In most ionic solids the contributions of the holes and electrons to the overall conductivity is negligible compared to those of ions. Assuming that only one type of mobile species makes a significant contribution to the observed conductivity, Eq. (1.1) becomes

$$\sigma = nq\mu \quad (1.2)$$

Where $q = ze$ (z is the valency of the mobile ion and e is the electronic charge).

In poor and moderate conductors the charge carriers are thermally induced interstitial ions (Frenkel defects) or vacancies (Schottky defects) in the crystal structure. The equilibrium concentration of either type of defects is given to a good approximation by

$$n = Bn_0 \exp[-G_s/(2kT)] \quad (1.3)$$

Where G_s is the energy of formation of a defect pair at the temperature T , n_0 the concentration of normal lattice site, and B is an entropy factor, which depends upon the crystal structure and the type of defect, involved [3].

The variation of mobility with temperature for poor and moderate conductors may be expressed as

$$\mu = \left(Aa^2 v \right) / (kT) \exp[-G_m/(kT)] \quad (1.4)$$

Where G_m is the free energy of migration of the mobile species through the lattice, v is the frequency of vibration, a is the jump distance, and A , a factor which accounts for the change in G_m with temperature [3].

Combining Eqs. (1.1), (1.2) and (1.3) one obtains a general expression for conductivity as follows

$$\sigma = (C/T) \exp[(-G_s/2 - G_m)/(kT)] \quad (1.5)$$

In terms of the corresponding enthalpy (H) and entropy (S),

$$G_s = H_s - TS_s \quad (1.6)$$

$$G_m = H_m - TS_m \quad (1.7)$$

Eqn. (1.5) can be rewritten as

$$\sigma = (\sigma_0/T) \exp[(-H_s/2 - H_m)/(kT)] \quad (1.8)$$

$$\text{or,} \quad \sigma T = \sigma_0 \exp[-E'_a/(kT)] \quad (1.9)$$

Where E'_a is the overall activation energy for conduction. Thus a plot of $\log(\sigma T)$ vs. $1/T$ is linear whose slope yields the overall activation energy E'_a . However, since the variation of $\log T$ over the experimental range (400K to 750K) is negligible in comparison to that of $\log \sigma$, a plot of $\log \sigma$ vs. $1/T$ is also found to be linear and is preferred because of its obvious simplicity. However, the activation energy E_a obtained from this plot is slightly lower than E'_a obtained from Eqn. (1.9) by an amount equal to the thermal energy (kT), i.e. $E_a = E'_a - kT$.

Generally a plot of $\log \sigma$ vs. $1/T$ for a normally pure ionic solid consists of two linear segments; a high temperature linear region that is an intrinsic property of the material, and a low temperature extrinsic region

characterized by a lower slope (hence lower activation energy). The intrinsic region relates to the temperature range in which the dominant defects are those, which are present due to thermodynamic considerations. In this case E_a is the sum of half the formation energy (H_f) and energy of migration (H_m) of defects. The extrinsic region relates to the temperature range in which dominant defects are those introduced by the addition of aliovalent impurities and are present due to charge neutrality conditions. Here E_a is simply the migration energy (H_m) alone.

The position of extrinsic –intrinsic transition temperature is known as knee temperature, and is often used as a measure of the impurity level in the crystal.

1.2 Classification of Solid Electrolytes

Solid electrolytes can be classified in many ways as discussed below:

1.2.1 Nature Dependent Classification

Depending on the nature of the material, the solid electrolytes can be grouped into the following three categories:

- (i) Crystalline
- (ii) Amorphous
- (iii) Heterogeneous

Crystalline Solid Electrolytes:

A great majority of the ionically conducting solids or solid electrolytes are crystalline in nature. A perfect crystalline material would be an insulator. The presence of defects or disorder is a necessity to sustain significant ionic transport. It is natural to classify the ionic solids according to the types of defect or disorder responsible for ionic transport [4]. These are principally of two types:

(1) Point defect type

In the point-defect-type solids, the transport is through Frenkel or Schottky defect pairs, which are thermally generated. The activation energy is generally high, $\sim 1\text{eV}$ or more. The point defect type solids can be further subdivided according to the defect concentration density as follows:

a) Dilute: The number of mobile defects $\sim 10^{18}\text{cm}^{-3}$ or less

Examples-AgCl, β -AgI, NaCl, KCl etc.

b) Concentrated: The number of mobile defects $\sim 10^{18}$ - 10^{20}cm^{-3}

Examples-Stabilized zirconia or hafnia, CaF_2 etc.

(2) Molten sub lattice type

The number of mobile defects $\sim 10^{22}\text{cm}^{-3}$.

In molten-sublattice-type solids, the number of ions of a particular type is less than the number of sites available for them in its sublattice. As a result, all these ions can hop or move like a free ion from one position to another. Since all these ions are available for transport, the conductivity is large and the activation energy is low. These materials possess an average structure rather than a rigid structure.

Examples: α -AgI, MAg_4I_5 ($\text{M}=\text{K}, \text{Rb}, \text{NH}_4$, etc.), α - Li_2SO_4 etc.

Amorphous Solid Electrolytes:

Amorphous solid electrolytes resemble more closely with liquid electrolytes than crystalline solids. They include:

Ionically conducting glasses, and

Ionically conductive polymers.

Polymers can be further classified depending on different ways the ions can be incorporated into the polymers. For example:

Gel polymer electrolyte, such as PVF_2 , $\text{PC} + \text{LiClO}_4$ etc.

Polymeric salt electrolyte such as Nafion.

Solvating polymeric electrolyte such as PEO + LiClO₄.

Heterogeneous Solid Electrolytes:

These comprise the solid electrolytes containing dispersion of a second phase, generally in the form of fine (submicron size) particles. The dispersed second phase can be an insulating oxide such as Al₂O₃, SiO₂, Fe₂O₃, ZrO₂, CeO₂ etc. or another ionic solid, such as β -Li₂SO₄-M₂SO₄ (M=Na, Rb, Cs).

1.2.2 Transition Dependent Classification

O'Keefe and coworkers [5] have divided ionic solids into three categories based on the nature of their phase transitions:

Class I:

These are “normally melting “ salts such as alkali halides which show large discontinuities in ionic conductivity at the melting point, with low conductivities but strongly temperature dependent (large activation energies, $\sim 1\text{eV}$) in the solid phase.

Class II:

These crystals show first-order solid electrolyte transitions. In a subclass IIa, O'Keefe placed those materials which show a large, discontinuous change in ionic conductivity and a change in the lattice symmetry of both mobile and non-mobile sublattices typified by the $\alpha \rightarrow \beta$ transition in AgI and Li₂SO₄.

In class IIb are placed those crystals for which the change in the immobile sublattices are minor, e.g. Ag₂HgI₄.

Class III:

This includes materials in which the change from low to high ionic conductivity is spread over a wide temperature range and there is no change in the symmetry of the non-conducting sublattice, e.g. PyAg₅I₆ [Py = C₅H₅NH].

Table 1.1:

A list of materials exhibiting the various types of transitions

CLASS I Normal melting:

Alkali halides, PbCl_2 , MgCl_2 , CaBr_2 , YCl_3 etc.

(O'Keefe and Hyde [5])

CLASS II First order transition:

Cationic conductors:

CuBr , CuI , AgI , Ag_2S , Li_2SO_4 , Li_2WO_4

(Takahashi [6])

Anion conductors:

LuF_3 , YF_3 , BaCl_2 , SrBr_2 , Bi_2O_3

(O'Keefe and Hyde [5])

CLASS III Faraday transition (diffuse)

Cation conductors:

Na_2S , Li_4SiO_4

(West [7])

Anion conductors;

CaF_2 , SrF_2 , LaF_3 , SrCl_2 , PbF_2 , CeF_3

(O'Keefe and Hyde [5]; Derrington *et al.* [8,9]; Nagel and O'Keefe [10])

The transition featured by class III materials is sometimes called a Faraday transition (Landau and Lifschitz [11]). Table 1.1 lists some of the typical examples of all these three types of materials.

1.3 Importance of Solid Electrolytes

Batteries employing liquid electrolytes [12] have the following drawbacks. They have

- (a). Limited temperature range of operation
- (b). Limited shelf life
- (c). Low energy density
- (d). Thin film construction is not possible
- (e). Cannot be charged or discharged quickly

Solid electrolytes are more advantageous than liquid electrolytes, for the following reasons. They have

- (a). Very high energy and power densities
- (b). Required no containers
- (c). Convenient for handling
- (d). Longer shelf life
- (e). Wide range of operation temperature

1.4 Maxwell Model for Composite Electrolytes

In the classical theory proposed by Maxwell the conductivity of a two-phase mechanical mixture has been calculated in terms of the bulk conductivities of the individual phases.

A composite electrolyte is having two constituents with mole fractions f_1 and f_2 . Let the conductivities of the first and second electrolytes are σ_1 and σ_2 respectively. Then according to Maxwell's classical theory conductivity of the composite electrolyte can be given by:

Lunden and coworkers have studied Li_2SO_4 and a large number of its solid solutions in great detail. According to Forland and Krogh-Moe [14], Li_2SO_4 is monoclinic at low temperature (β -phase): $a=8.239\text{\AA}$, $b=4.9536\text{ \AA}$, $c=8.4737\text{\AA}$ and $\beta=107.98^\circ$ at 298K. The structure of the high temperature (α -phase) modification of Li_2SO_4 is fcc with SO_4^{2-} ions [4] situated at the origin and the oxygen atoms rotationally disordered about the sulphur atom. The structure of α - Li_2SO_4 is shown in Fig. 1.2. According to Forland and Krogh Moe the sulphate ions are arranged in a pseudo-cubic face-centered lattice with lattice parameter $a=7.07\text{\AA}$ at 610°C . Oye [16] has suggested that every second layer of sulphate ions is rotated 90° around the Z-axis. For every sulphate ion there are three cation sites: two tetrahedral sites at $(1/4, 1/4, 1/4)$ and $(3/4, 3/4, 3/4)$ with a free space of 1.42\AA and one octahedral site at $(1/2, 1/2, 1/2)$ with a free space of 2.76\AA . These free spaces provide sufficient open structure for the motion of Li^+ ions. There is only one formula unit of Li_2SO_4 associated with every lattice point, and thus there is an excess of available cation sites (3 sites for each of two cations).

Rheological studies have shown that fcc Li_2SO_4 can be characterized as a plastic crystal. The appearance of a plastic phase is considered being part of the melting process, i.e. it is a pre-melting phenomenon shown by the crystal lattice [17]. The plastic phases was found to be thixotropic with a slow regeneration. This high temperature phase, which exists between the $\beta \rightarrow \alpha$ transformation temperature (575°C) and the melting point at 860°C , has a clear glassy appearance (Jansson and Sjoblom [17]). The latent heat of phase transformation is 27 kJ/mole while the heat of melting is only 8 kJ/mole [18]. Such a high value is typical for the transformation to the plastic, so called rotor phases, found for some organic compounds. At the solid-solid

phase transformation the volume of Li_2SO_4 increases by $\sim 3.2\%$ while the increase at the melting point is very small [19].

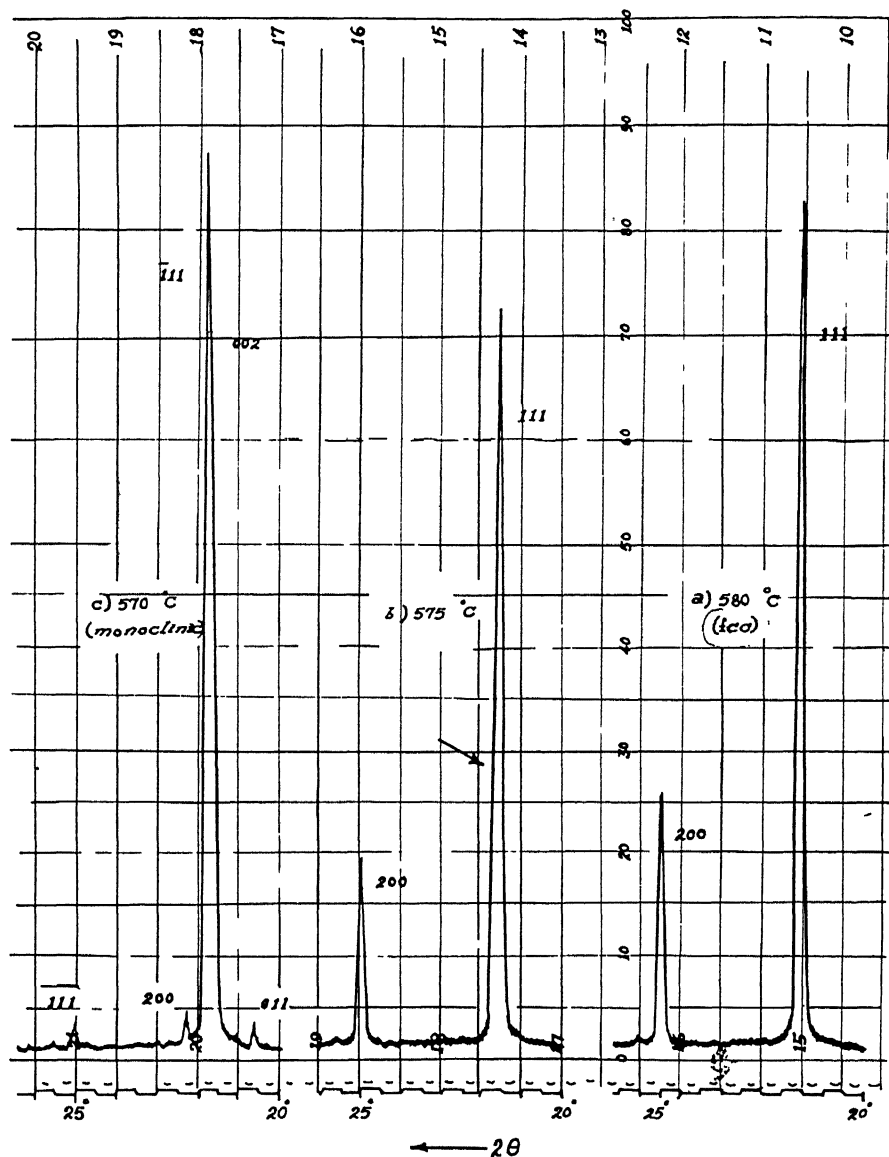


Fig. 1.1: Structural phase transition of Li_2SO_4

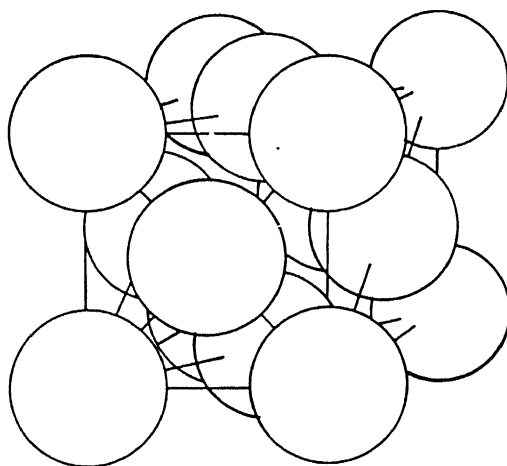
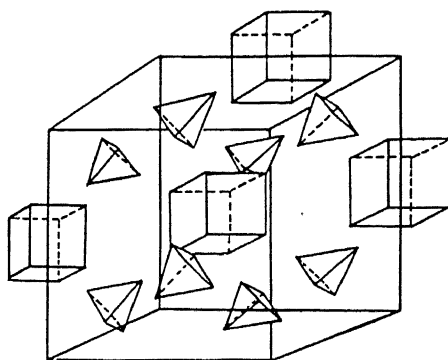


Fig. 1. 2: Structure of α - Li_2SO_4

Sulphate systems have been pursued with considerable interest due to their potential applications in various electrochemical devices. The cell/batteries utilizing α -Li₂SO₄ as the solid electrolyte have been studied. The large heat content of the solid-solid phase transition is proposed to be utilized for heat storage by Schroeder and Sjoblom [20] and Sjoblom [21]. Another application of sulphate-based electrolytes is in the devices like gas sensors for monitoring the concentration of SO₂ and SO₃ in the environment and elsewhere.

1.7 Recent progress

The ionic conduction mechanism of high-temperature sulfate phases Li₂SO₄, LiNaSO₄, LiAgSO₄ and Li₄Zn(SO₄)₃ has been extensively studied and discussed for many years. Two mechanisms named as 'paddle-wheel' and 'percolation' mechanisms were presented for ionic migration. In the recent paper published by Meng *et al.*[22], Zn²⁺ ion was selected as dopant for Li₂SO₄ and the transport mechanism is discussed through the investigation of conductivity change. The results show that the conductivity of all Zn²⁺ containing samples is higher than β -Li₂SO₄ (Al₂O₃) below 500°C. While above 550°C the samples display higher conductivity than that of α -Li₂SO₄. However, the conductivity value decreases first when the amount of Zn²⁺ is less than 4 mol%, and then increases and reaches a maximum point around 7 mol% Zn²⁺ or 7 mol% ionic vacancies. This observation indicates that both paddle-wheel and percolation mechanisms seem to contribute to the ionic conduction in α -Li₂SO₄.

Although H₂/O₂ fuel cells using Li₂SO₄ as the electrolyte have encountered problems in their chemical instability, the Li₂SO₄ electrolyte shows an excellent chemical stability under the operational conditions of a fuel cell using H₂S as the fuel (Zhu *et al.*[23]). Both thermodynamic analysis

and experiments have demonstrated that it is feasible to develop practical $\text{H}_2\text{S}/\text{O}_2$ fuel cells and co-generation devices based on the Li_2SO_4 electrolyte.

Electrical conductivity and dielectric relaxation studies on a large number of lithium ion conducting glasses belonging to the ternary glass system $\text{Li}_2\text{SO}_4\text{-Li}_2\text{O-P}_2\text{O}_5$ has been carried out over a wide range of temperature (150 K to 450 K) and frequencies (10 Hz- 10^7 Hz). DC conductivities exhibit two different activation regions. This seems to be suggestive of the presence of a cluster-tissue texture in these glasses. The clusters may be of both Li_2SO_4 and lithium phosphate and are held together by a connective tissue of average composition. This conjecture seems to be well-supported by the ac conductivity behaviour of these glasses which have been analyzed using both power law and stretched exponential relaxation functions (Ganguli *et al.*[24]).

El-Rahmana *et al.*[25] have studied the electrical conductivities(σ) of polycrystalline Li_2SO_4 and Ag_2SO_4 in the temperature ranges 310-950 and 370-730 K, respectively. An increase in the magnitude of followed by a change in the slope of $\ln\sigma T$ against T^{-1} plots is observed around 860 and 714 K for Li_2SO_4 and Ag_2SO_4 , respectively, which correspond to the phase transition temperatures (T_p) from the normal ionic solid (β -phase) to the superionic conducting phase (α -phase). The activation enthalpies of the superionic phase and the enthalpies of formation of defects and association were evaluated and discussed from the temperature variation of σ . The specific heat capacity (C_p), total thermal conductivity (λ_t) and thermal diffusivity (a) were measured for polycrystalline Li_2SO_4 and Ag_2SO_4 in the temperature range 290-635 K. The radiative pulse heat technique was used for the measured thermal properties. The results indicated that the

mechanism of heat transfer is due mainly to phonons. The roles of photons and bipolars are negligible in the investigated temperature range.

The thermal conductivity and diffusivity of lithium sulphate have been measured simultaneously, using the transient plane source technique over the temperature range 300-900 K (Suleiman *et al.*[26]). The thermal conductivity decreases slowly up to about 640 K, whereupon a distinct rise occurs, indicating the onset of a pre-transitional behaviour, which causes a continuous growth of the conductivity up to the structural phase transition at 851 K, whereupon a very sharp increase occurs. A similar behaviour has been observed for the thermal diffusivity, for which a very sharp dip occurs at the transition point due to the exceptionally large transition enthalpy. The pre-transitional behaviour of heat transport is associated with the librational disorder of the sulphate anions known from Raman scattering studies of both phases (and neutron scattering from the cubic phase), whereas the translational disorder of lithium cations is of hardly any importance. It is thus possible to link the 'paddle-wheel' concept of ion migration in the cubic phase to the enhancement of heat transport observed in the 'pre-transition' region, as well as to the large difference in heat-transport rates between the monoclinic and cubic phases.

Emf measurements were made on the cell without liquid junction: Li-ISE LiCl(m_1), Li₂SO₄(m_2) Ag/AgCl. The performances of the electrode pairs constructed were tested and exhibited near Nernstian behavior (Yan *et al.*[27]). The mean activity coefficients of LiCl for the system Li⁺-Cl⁻-SO₄²⁻-H₂O have been investigated by the emf values at temperatures of 0, 15, 35°C and constant total ionic strengths of 0.05, 0.1, 0.5, 1.0, 2.0, 3.0 and 5.0 mol·kg⁻¹. The activity coefficients decrease with increasing temperature and the ionic strength fraction of Li₂SO₄ in the mixtures. The thermodynamic

properties are interpreted by use of Harned's empirical equations and Pitzer's ion interaction approach including the contribution of higher order electrostatic terms. The experimental results obey Harned's rule and are described by using Pitzer equations satisfactorily. The activity coefficients of Li_2SO_4 , the osmotic coefficients and the excess free energies of mixing for the system in the experimental temperature range were reported.

The analysis of the solubility of MSO_4 in the high-temperature cubic modification of Li_2SO_4 reveals that divalent cations in the Li_2SO_4 structure can occupy either tetrahedral or octahedral positions (Fedorov [28]). The former case is preferred for Be^{2+} , and, to some extent, for Zn^{2+} . For all the other divalent cations the octahedral positions are preferred in the formation of the $\alpha\text{-Li}_2\text{SO}_4$ -based solid solutions.

Uvarov *et al.*[29]) have studied the morphology, crystal structure, chemical content, thermal and transport properties of $\text{Li}_2\text{SO}_4\text{-Al}_2\text{O}_3$ composites prepared in two different ways: by thermal decomposition of the precursor $\text{Li}_2\text{SO}_4\cdot 2\text{Al}(\text{OH})_3\cdot m\text{H}_2\text{O}$ at 400°C or by using conventional mixing. It is shown that, whatever the preparation technique, if grain size of alumina in composites is small enough (of order of tens nanometers) then after prolonged heating the heterogeneous system $\text{Li}_2\text{SO}_4\text{-Al}_2\text{O}_3$ reaches the metastable thermodynamic state - a nanocomposite in which lithium sulphate is in an unusual epitaxial state. The stabilization of this state is caused by a strong interface interaction that is leading to the formation of the intermediate thin layer of lithium aluminate, which 'glues' Li_2SO_4 and Al_2O_3 phases providing the contact. The phase transition temperature of Li_2SO_4 in composites is 100 degrees lower than in the pure salt. Ionic conductivity of Li_2SO_4 in the composites smoothly changes at the phase transition, activation energies being 0.40 ± 0.05 and 0.66 ± 0.01 eV for $T > 470^\circ\text{C}$ and

$T < 280^{\circ}\text{C}$, respectively. The value of the charge carrier concentration in the nanocomposites estimated from the frequency dependent conductivity turned out to be comparable with that in glasses and superionic conductors.

Lithium sulphate and a few other compounds have high temperature phases, which are both solid electrolytes and plastic crystals (rotor phases). Three types of experiments are considered in order to test the validity of a 'paddle-wheel mechanism' that has been proposed for cation conductivity in these phases (Andersen *et al.*[30]). A single-crystal neutron diffraction study has been performed for cubic lithium sulphate. The refinement of the data gives a very complex model for the location of the lithium ions. There is definitely a void at and near the octahedral ($[\frac{1}{2}, \frac{1}{2}, \frac{1}{2}]$) position. 90% of the lithium ions are located at the tetrahedral 8c-sites ($[\frac{1}{4}, \frac{1}{4}, \frac{1}{4}]$), although significantly distorted in the directions of the four neighbouring sulphate ions. The remaining 10% of the lithium ions are refined as an evenly distributed spherical shell, which is surrounding the sulphate ions. The lithium ions are transported along a slightly curved pathway of continuous lithium occupation corresponding to a distance of about 3.7 angstrom. Thus, lithium transport occurs in one of the six directions $[110]$, $[11\text{ over-bar }0]$, $[101]$ etc. The electrical conductivity has been studied for solid solutions of lithium tungstate in cubic lithium sulphate. The conductivity is reduced in the one-phase region, while it is increased in a two phase (solid-melt) region. There are pronounced differences between the rotor phases and other phases concerning how partial cation substitution affects the electrical conductivity of solid solutions. Regarding self and interdiffusion, all studied mono- and divalent cations are very mobile in the rotor phases, which lack the pronounced correlation with ionic radii that is characteristic for diffusion in other classes of solid electrolysis. The quoted

CHAPTER 2

Experimental Details and Characterization Techniques

2.1 Experimental set up

2.1.1 Sample holder

The sample holder used for the conductivity experiments is shown schematically in Fig.2.1. It essentially consists of three identical lava discs (diameter ~ 2.5 cm and thickness ~ 1 cm), each having a central hole and four symmetrically located holes near the periphery. The lava discs, after machining were heated slowly to 1000°C and kept at that temperatures for two hours before cooling inside the furnace. This kind of heat treatment was necessary to harden the lava disc and also to remove any moisture content. The effect of latter was to increase the resistivity of the disc significantly. Pair of stainless steel rods was passed through the two diametrically opposite holes to provide support to the sample holder. The spring which was so located that it remains outside the furnace, applied uniform pressure due to spring action to ensure a firm contact between the electrodes and the sample. A quartz tube was used to provide the body of the sample holder.

The flat surfaces of the cylindrical pellets were polished on different grades of fine polishing papers to remove the surface contamination and to obtain smooth and parallel surfaces. The surfaces were then coated with graphite paint, which will act as the electrodes. The pellet was carefully placed between the two silver electrodes. The spring mechanism ensures that there was a firm and uniform contact between the electrodes and the sample, at all temperatures.

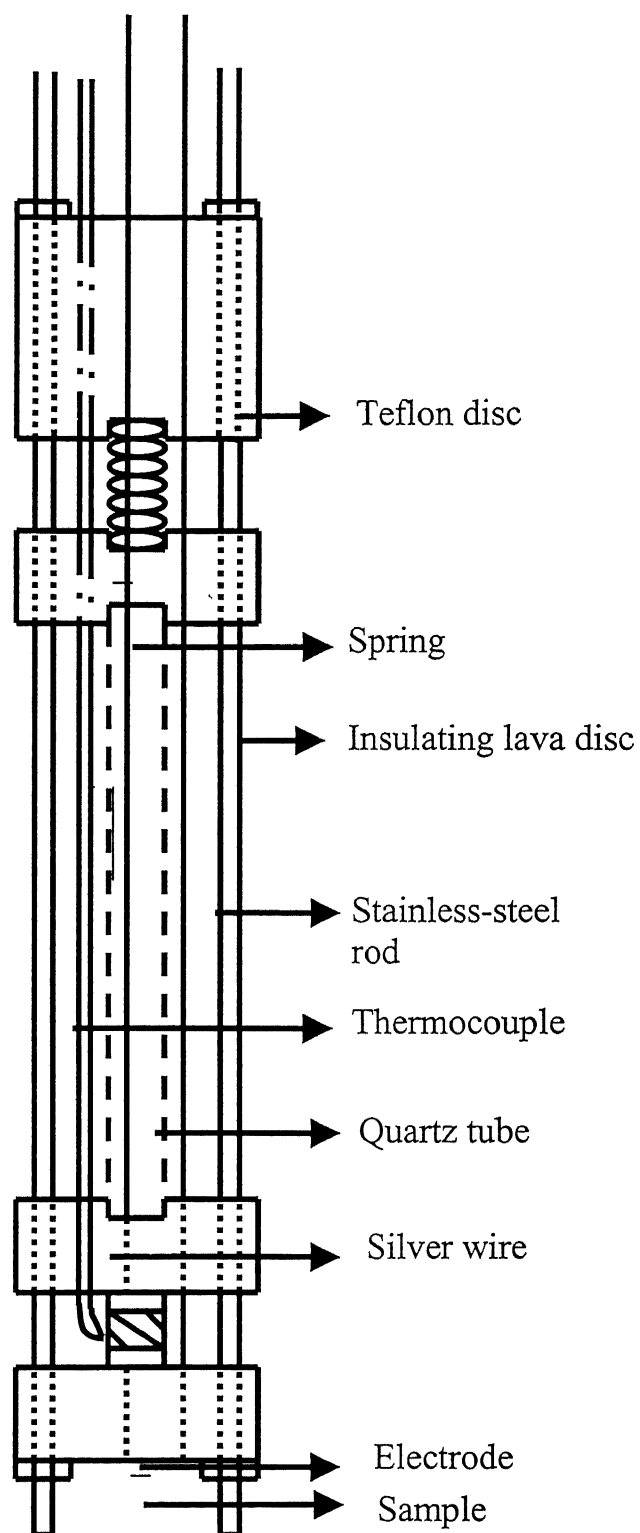


Fig.2.1: Sample holder for complex impedance analysis

2.1.2 Furnace and Temperature Controller

An electrical resistance heating furnace comprising a mullite tube (internal diameter ~ 4.9 cm), over which kanthal wire was wound uniformly, has been used. The resistance of the heating element was 28.2Ω . A high temperature cement was applied over the kanthal to fix it at place. The mullite tube with cemented kanthal wiring was enveloped with a cylindrical stainless steel container and the space between mullite tube and steel container was filled with glass wool in order to minimize the heat loss.

A chromel-alumel thermocouple was employed to measure the temperature of the sample. A DMM is connected to output of this thermocouple and moreover a PID type temperature controller (Indotherm 401D) has been used to control the temperature of the furnace. A platinum-13% rhodium thermocouple has been used for providing feedback to the temperature controller, which compares set temperature & actual temperature and accordingly supplies the required power to the furnace. The accuracy of the DMM used is $1 \mu\text{V}$.

2.1.3 Impedance Analyzer

A HP 4192A fully automatic impedance analyzer along with a HP 1607A- test fixture is employed for a wide range of complex impedance measurement. Impedance analyzer is a small-signal ac measurement device with a wide range of frequencies to investigate the electrochemical properties of the solid electrolytes. The instrument has an auto balancing bridge with a test signal from 5 mV to 1 mV. One can sweep the frequency from 5 Hz to 13 MHz. The two display modes 'A' or 'B' can be selected to measure the quantities of interest as in table 2.1. Usually one uses a parallel mode of connection so that the resultant semicircle plot of $|Z\cos\theta|$ and $|Z\sin\theta|$ can be utilized for calculating the resistance of the various

components present in the circuit. Depending upon the presence of interfacial capacitance, and grain boundaries, the plot takes different shapes.

Table 2.1: The Displays ‘A’ and ‘B’ of Impedance Analyzer

Display A Function	Display B Function
Z : Absolute value of Impedance Y : Absolute value of Admittance	θ (deg/rad): Phase angle
R: Resistance	X: Reactance
G: Conductance	B: Susceptance
L: Inductance C: Capacitance	Q: Quality Factor D: Dissipation Factor R: Resistance G: Conductance

The equivalent circuit modes are auto, series or parallel and one can select depending upon ones interest.

2.1.4 Experimental arrangement

The block diagram in Fig.2.2 shows the experimental set up for the conductivity experiments. The sample whose electrical and dielectric properties are to be measured is made in the form of a pellet by applying a force of 4 tons. After applying necessary graphite coating, the pellets are placed between the silver electrodes of diameter 11mm in the sample holder. The silver electrodes are brazed (using gas welding) to silver wires to provide connection to the impedance analyzer, and chromel–alumel thermocouple is attached with the sample holder to measure the temperature of the sample, which is connected to a Kiethly DMM (Digital Multi Meter) which will measure the temperature as a function of voltage. From the calibrated tables one can calculate the temperature of the sample. A

temperature controller (Indotherm 401D) is used to control the furnace temperature. The various components of this set up were discussed in detail above.

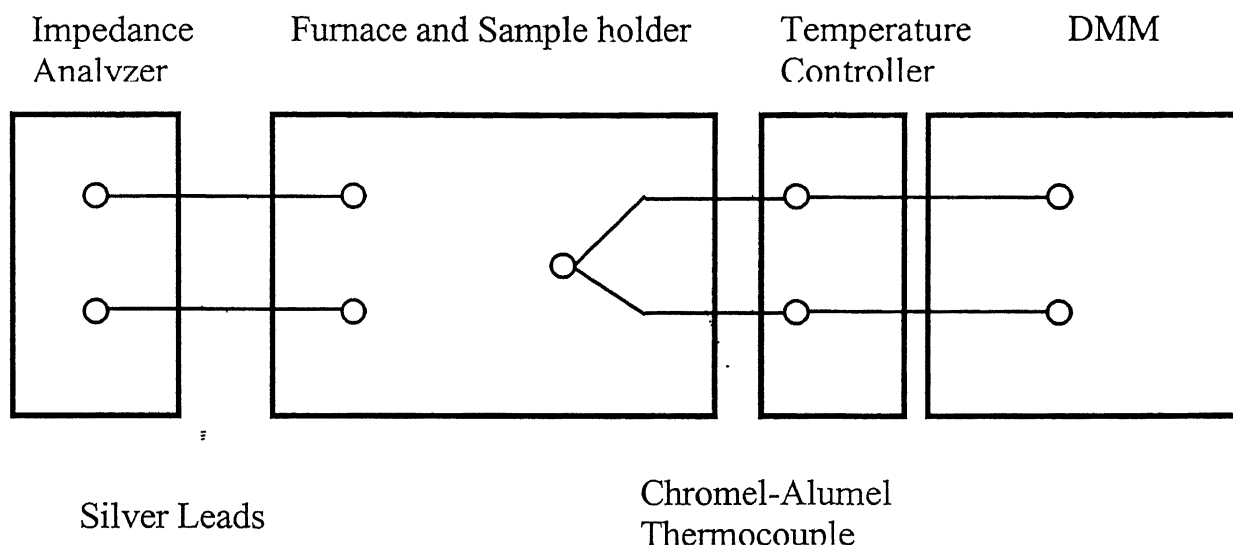


Fig.2.2: Block diagram of the experimental set-up used in the ionic conductivity measurements

2.2 Structural Analysis by X-Ray Diffraction (XRD)

A knowledge of different phases present in a material is important to understand the electrical properties. For example β - Li_2SO_4 is a poor ionic conductor at room temperature, but α - Li_2SO_4 is a superionic conductor [4]. In order to identify the various phases present in the samples containing the various mole fractions of Li_2SO_4 and FeSO_4 , X-ray diffraction patterns have been taken and analyzed.

The X-ray diffraction patterns of various compositions were recorded using a computerized Richeifert (ISO-DEBYEFLEX 2002) powder diffractometer using a filtered CuK_α ($\lambda = 1.542 \text{ \AA}$) radiation. The generator

was operated at 30 kV and 20 mA. The scanning speed was 3°/min in 2 θ . All XRD patterns were recorded at room temperature.

2.3 BET Measurement

The BET (Brunauer, Emmet and Teller) calculation was first introduced in 1938. It is the most commonly used technique to determine the specific surface area. The BET surface area (which includes all internal structure) is calculated from a multiplayer adsorption theory. The method may be defined simply as the physical characterization of material structures using a process where gas molecules of known size are condensed and the resultant sample pressure are recorded and used for subsequent calculation. This data, when measured at constant temperature, allows an isotherm to be constructed. Isotherm data is then subjected to a variety of calculation models to obtain surface area.

The BET equation should produce a straight line plot, the linear form of which is most often represented as:

$$\frac{P_s}{V_A(P_o - P_s)} = \frac{1}{V_M C} + \left[\frac{C-1}{V_M C} \right] \times \frac{P_s}{P_o} \quad (2.1)$$

Where: V_M = volume of monolayer

V_A = volume adsorbed

P_s = sample pressure

P_o = saturation pressure

C = constant related to the enthalpy of adsorption

A specified relative pressure range (usually 0.05 to 0.2) is chosen and the isotherm data is used to calculate the BET function, which is plotted against relative pressure (P_s/P_o). This plot is often a straight line having a slope $(C-1)/V_M C$ and intercept $1/V_M C$.

The BET surface area in (m^2/g) is then determined from the following expression:

$$S_{\text{BET}} = \frac{V_{\text{M}} \times N_{\text{A}} \times A_{\text{M}}}{M_{\text{V}}} \quad (2.2)$$

Where S_{BET} is the BET surface area, N_{A} is Avogadro number, A_{M} is the cross sectional area occupied by each adsorbate molecule, and M_{V} is the gram molecular volume (22414mL). For nitrogen BET determination, the cross-sectional area of the adsorbate molecule is assumed to be 0.162 nm^2 .

2.4 Fourier Transform Infrared Spectroscopy (FT-IR)

The broadband spectra like Raman and IR are presently becoming increasingly useful tools to study the structural aspects of the material under study, which are sensitive to compositional variations. Infrared spectroscopy, in particular, involves the absorption of electromagnetic radiations by matter, the existence of which is known since a long time [34] with the discovery of Sir William Herschel in 1800. Today infrared spectroscopy ranges approximately from $0.78\mu\text{m}$ ($1/\lambda = 12500\text{cm}^{-1}$) to $1000\mu\text{m}$ ($1/\lambda = 10\text{cm}^{-1}$). However the most useful range is from $2\mu\text{m}$ to $16\mu\text{m}$. The absorption bands, which occur in this region, are due to the fundamental molecular vibrations. Consequently they lend themselves to identification, qualitative analysis and band alignment.

It is well accepted fact that the matter absorbs infrared radiations selectively with respect to the wavelength. The two necessary conditions, which must be met before the absorption of infrared radiations by the molecule can occur, are

- 1) There must be a change in dipole moment of a molecule, and this will occur only when the electrical charges on the atoms are unequally distributed. Under these conditions, a stationary alternating electric

field is produced whose magnitude changes with frequency; and it is this electric field, which interacts with the field of electromagnetic radiations.

- 2) The molecular vibration frequency must be identical to that of incident electromagnetic radiation, failing which the radiations transmit through the molecule without any loss of energy.

As a result, when infrared radiations of successive frequencies are passed through the molecules and the fraction of transmitted energy is plotted against the frequency or wavelength, the result is a series of minima and maxima, which is referred to as an infrared absorption spectrum. The absorption or transmission of this electromagnetic energy is dependent on the number of atoms, their mass, their way of stacking in the material and the force constant of interatomic bonds. The vibrations between various atoms within the molecule could be described as stretching vibrations, bending vibrations, involving groups of atoms within the molecule and the vibrations of the molecule as a whole. These vibrations can occur at various frequencies and are characteristics of groups of atoms within the molecule. Thus, absorption peaks at various wavelengths are correlated with the molecule, using which, the structural studies can be carried out. The depth of the absorption bands is directly related to the number of molecules in the beam of radiation, and this feature is often used for qualitative measurements.

The samples were prepared by grinding and then mixing thoroughly in an agate mortar. The Fourier Transform Infrared Spectroscopy (FT-IR) studies were carried out with a spectrometer model Vector-22(Bruker) in the range $400\text{-}4000\text{cm}^{-1}$. Measurements were made on an amorphous

material dispersed in KBr in the ratio 1:30. Pure Li_2SO_4 and $\text{Li}_2\text{SO}_4+0.2 \text{FeSO}_4$, $\text{Li}_2\text{SO}_4 +0.3 \text{FeSO}_4$, $\text{Li}_2\text{SO}_4 +0.4 \text{FeSO}_4$ were analyzed.

2.5 Complex Impedance Analysis

Impedance spectroscopy (IP) is a relatively new and powerful method of characterizing many of the electrical properties of materials and their interfaces with electronically conducting electrodes [35]. It may be used to investigate the dynamics of bound or mobile charge in the bulk or interfacial regions of any kind of solid or liquid material: ionic, semiconducting, mixed electronic-ionic, and even insulators (dielectrics). The complex impedance data analysis can yield near-perfect estimates of bulk conductivity of the materials free from the electrode polarization effects, which are obtained from the steady state dc measurements. Impedance spectroscopy was first applied by Baurle (1969) to study the basic polarization process in the cell of yttria stabilized zirconia. Since dc measurements involve polarization effects, ac measurements are preferred to extract the dc conductivity.

Impedance of a circuit is the ratio of voltage to the current as Ohm's law holds well in the time domain. If the voltage function is given by

$$V(t) = V_m \exp(j\omega t) \quad (2.3)$$

then the current function will be given by:

$$I(t) = I_m \exp[j(\omega t + \phi)] \quad (2.4)$$

The impedance of the circuit, $Z(\omega)$, has both magnitude $|Z|$, and phase angle ϕ and can be expressed in both polar and Cartesian form;

$$\begin{aligned} Z(\omega) &= |Z| \exp(-j\phi) \\ &= |Z| \cos\phi - j|Z| \sin\phi \\ &= Z' - jZ'' \end{aligned} \quad (2.5)$$

where Z' and Z'' are real and imaginary parts of the complex impedance. Therefore the magnitude of complex impedance

$$|Z| = \sqrt{Z'^2 + Z''^2} \quad (2.6)$$

and the phase angle is given by

$$\phi = \tan^{-1}\left(\frac{Z''}{Z'}\right) \quad (2.7)$$

$$\text{Admittance, } Y = 1/Z(\omega) = G + jB \quad (2.8)$$

$$\text{Conductance, } G = \frac{Z'}{Z'^2 + Z''^2} = \frac{1}{R} \quad (2.9)$$

$$\text{Susceptance, } B = \frac{Z''}{Z'^2 + Z''^2} = \omega C \quad (2.10)$$

The different types of contributions coming from the leads, electrolyte and the electrodes can be modeled as a combination of resistors and capacitors. The plot of Z' vs. Z'' for various representative circuits are described below.

2.5.1 Pure Resistive Circuit

The real and imaginary parts of the complex impedance of a purely resistive circuit, with resistance R are given by

$$Z' = R, Z'' = 0 \quad (2.11)$$

The impedance plot i.e., the plot of Z'' vs. Z' will be a point at $Z' = R$. Impedance plot for a purely resistive circuit is given in Fig. 2.3.

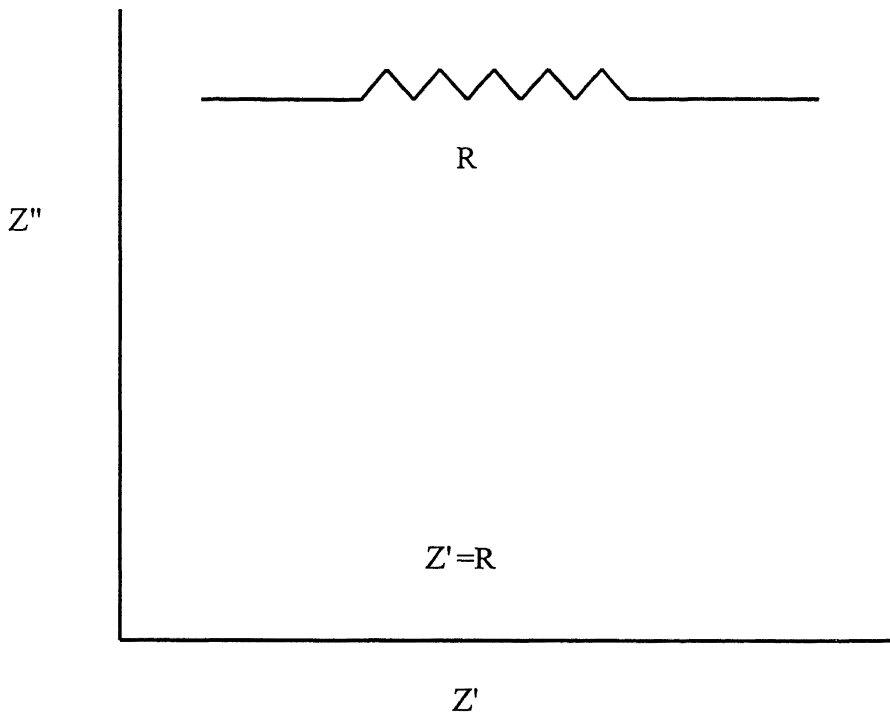


Fig. 2.3: Impedance plot for a purely resistive circuit

2.5.2 Pure Capacitive Circuit

For a purely capacitive circuit, the real and imaginary parts of complex impedance are given by

$$Z' = 0; Z'' = -1/\omega C \quad (2.12)$$

The corresponding impedance plot will be a straight line parallel to negative Z'' axis at $Z' = 0$. The impedance plot for a purely capacitive circuit is given in Fig. 2.4.

2.5.3 Series Combination of R and C

When the components behaving like a series combination of R and C, one gets

$$Z(\omega) = R - \frac{j}{\omega C} \quad (2.13)$$

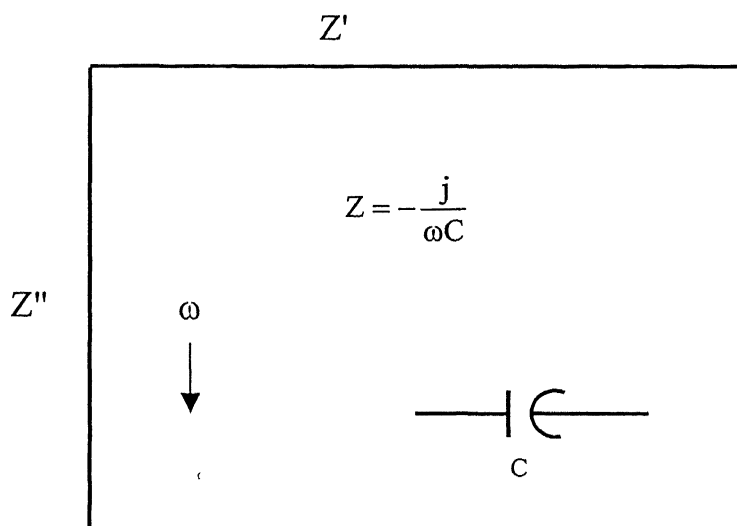


Fig. 2.4: Impedance plot for a purely capacitive circuit

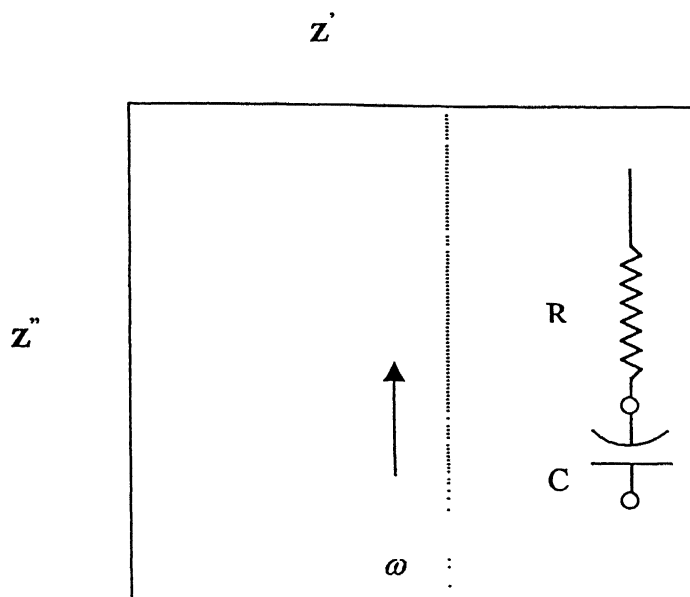


Fig. 2.5: Impedance plot for a resistor and a capacitor in series

$$Z = -\frac{j}{\omega C} \quad (2.14)$$

with $Z' = R$

$$Z'' = -\frac{1}{\omega C} \quad (2.15)$$

This essentially gives a straight line parallel to the negative imaginary axis at $Z' = R$, as shown in Fig.2.5

2.5.4 Parallel Combination of R and C

If the system of various components can be modeled as a parallel combination of R and C, then we get

$$Z(\omega) = \frac{R \left(\frac{1}{j\omega C} \right)}{R + \left(\frac{1}{j\omega C} \right)} \quad (2.16)$$

$$= \frac{R}{1 + \omega^2 C^2 R^2} + j \left[\frac{-\omega C R^2}{1 + \omega^2 C^2 R^2} \right] \quad (2.17)$$

Thus the real and imaginary parts of the complex impedance are

$$Z' = \frac{R}{1 + \omega^2 C^2 R^2} \quad (2.18a)$$

$$Z'' = -\frac{\omega C R^2}{1 + \omega^2 C^2 R^2} \quad (2.18b)$$

Eliminating ω from these two equations, Eqn.2.18a and 2.18b, and rearranging, it follows that

$$Z'^2 + Z''^2 = R Z' \quad (2.19)$$

or $(Z' - \frac{R}{2})^2 + Z''^2 = (\frac{R}{2})^2 \quad (2.20)$

This is the equation of a circle with radius $R/2$ with its center at $(Z' = R/2, Z'' = 0)$. The coordinates at the top of the arc will be $(R/2, R/2)$.

Since $Z'' = Z' = R/2$ at frequency ω_0 , equations (2.18) can be rearranged to give

$$\omega_0 RC = 1 \quad (2.21)$$

Thus, the impedance response of the resistor in parallel with a capacitor will be a perfect semicircle intersecting the real axis at R and 0 . The relaxation time, $\tau_0 = 2\pi RC$, for the circuit is given by the inverse of the frequency at the top of semicircle, ω_0 . Therefore the diameter of the circle is the dc resistance of the sample. The impedance plot when they are connected in parallel is shown in Fig. 2.6(a).

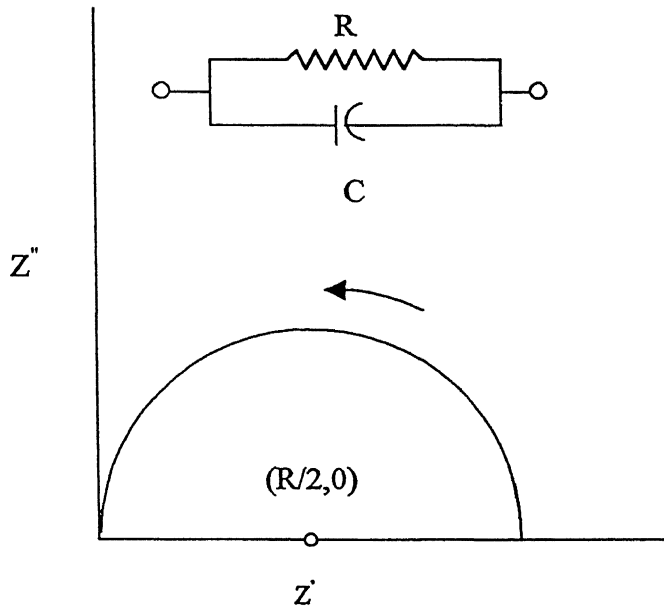


Fig. 2.6(a): Impedance plot for a resistor and a capacitor in parallel

When blocking electrodes are used, an electrode/electrolyte interface capacitance comes into play. This is attributed to the roughness of the electrode-electrolyte interface, the slope of the line decreasing with increasing roughness and a 90° angle of inclination is obtained only for

perfectly flat surfaces as shown in Fig. 2.6(b). This type of frequency response can be represented by a constant phase element (CPE) which has an impedance $Z = A(j2\pi f)^{-n}$, where n has a value between 0 and 1 and A is a constant.

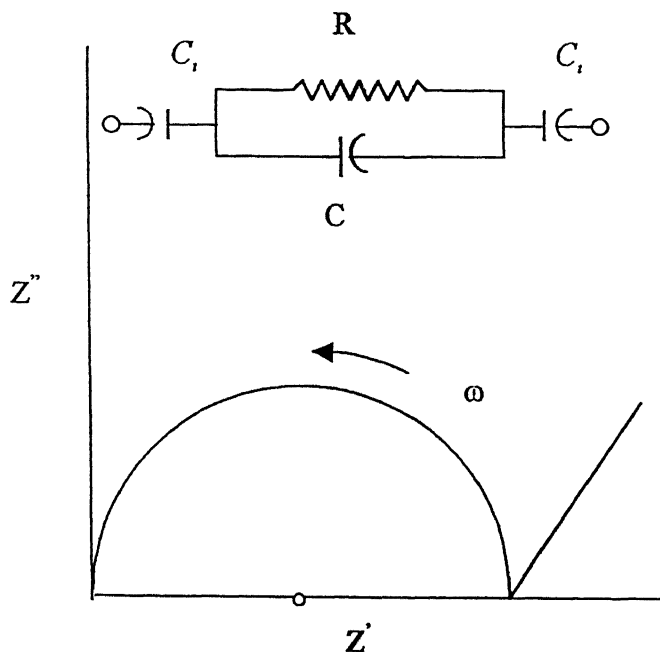


Fig. 2.6(b): Effect of interface capacitance C_i on impedance of electrolyte

In polycrystalline materials, there may be a contribution to the impedance due to the presence of grain boundaries. The grain boundaries may act as a hindrance to the ion transport, but they might also provide a high conductivity path since the defect density may be larger in the interface region. In the first case one can, in some cases, detect a second semicircle in the impedance plot representing grain boundaries [36,37]. The bulk resistance in such a case is obtained from the intersection of the high frequency impedance semicircle (Fig. 2.6(d)) with the real axis. If we have an increased conductivity at the grain boundaries it will give an apparent

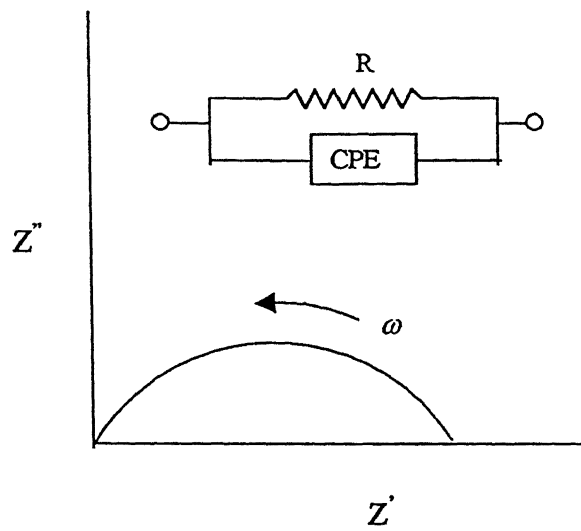


Fig. 2.6(c): Depression of Semicircle

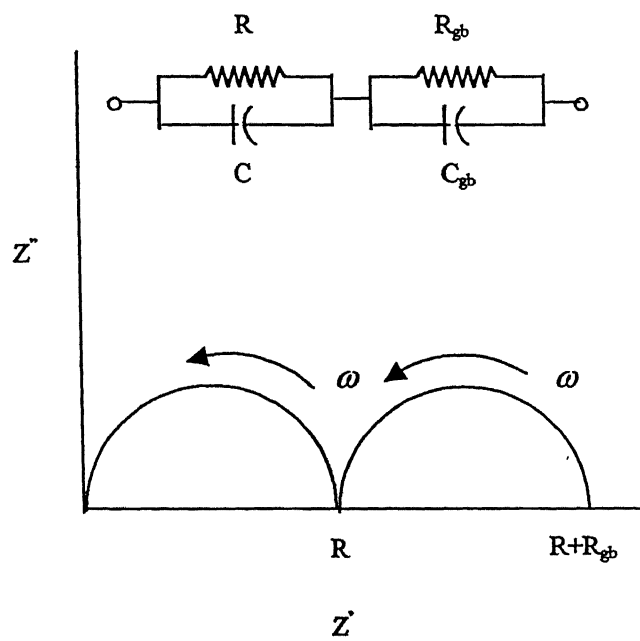


Fig. 2.6(d): Grain boundary effect

bulk conductivity dependence on grain size may help identify the conductivity mechanism if single crystals are not available. Another common impedance behavior is one in which the high frequency semicircle portion of the plot is depressed so that the center of the circle is situated below the real axis (Fig. 2.6(c)). It has been shown that in this case a CPE connected in parallel with the bulk resistance will result in such a depressed semicircle [38, 39].

2.6 Impedance Measurement Methodology

The impedance measurements for all compositions were carried out using HP 4192A impedance analyzer. The sample made in the form of pellet is loaded in the furnace using a specially designed sample holder. The spot frequency (f) was swept from 1 kHz to 13 MHz for a fixed temperature and values of Z , θ have been noted down. Impedance plots (Z'' vs. Z') have been drawn using the Microcal origin 6.0 software to ensure that proper points are available. The dc resistance (R_{dc}) have been calculated wherever circular plots are available. The diameter of the semicircle has been considered as R_{dc} . Using this R_{dc} one can calculate the dc conductivity (σ_{dc}) using the geometrical factor (l/A) of the sample as given below:

$$\sigma^* = \frac{l}{R_{dc}A} \quad (2.22)$$

Wherever the impedance plots are not circular, $\frac{Z}{\cos\theta}$ at 10 kHz has been used as R_{dc} . This can be explained further as follows:

The conductivity can be given as,

$$\sigma^* = \frac{l}{Z^*A} \quad (2.23)$$

$$= \frac{l}{(Z' + Z'')A} \quad (2.24)$$

$$= \frac{l}{(Z'^2 + Z''^2)A} (Z' - jZ'') \quad (2.25)$$

Therefore the real part of the conductivity (σ_R or σ_{dc}) can be given as

$$\sigma_{dc} = \frac{l}{(Z'^2 + Z''^2)A} Z' \quad (2.26)$$

$$= \frac{l}{(Z^2)A} Z' \quad (2.27)$$

$$= \frac{l}{Z^2 A} Z \cos\theta \quad (2.28)$$

$$= \frac{l \cos\theta}{ZA} \quad (2.29)$$

$$= \frac{l}{Z/\cos\theta \cdot A} \quad (2.30)$$

Therefore $Z/\cos\theta$ can be used in place of R_{dc} .

2.7 Materials processing

The physical properties of the starting materials Li_2SO_4 and FeSO_4 used are given below in table 2.2.

Table 2.2 The Physical Properties of the Starting Materials

	Li_2SO_4	FeSO_4
Supplier	Idrich Chemical Comp., USA	Qualigens Fine Chemicals, Mumbai
Purity	99%	98+%
Molecular Weight	109.94	151.96
Density (gm/cc)	2.20	
Melting point (K)	1118	

2.8 Sample Preparation

The starting materials Li_2SO_4 and FeSO_4 before use were dried and stored in an oven around 100°C to prevent the samples from absorbing the moisture. The mixed crystals of different compositions were prepared by weighing appropriate amount of materials in an electronic balance. The mixtures were then again dried to remove any moisture and then transferred to an agate mortar. The samples were powdered very well and then mixed properly to make it a homogenized mixture. The mixed powder is then transferred to a steel die of diameter 11 mm and placed over a hydrostatic press. A force of 4 tons was applied on each sample. The resulting pellets were placed in an aluminum crucible, which is then loaded in a furnace for sintering. All samples were sintered for 10 hours in an automated furnace. The rate of heating and cooling was kept at $1.5^\circ\text{C}/\text{minute}$. The sintered samples were then coated with graphite paint which acts as the electrodes for the electrical experiments. The sample holder loaded with such samples and chromel-alumel thermocouple was then placed inside the furnace and subsequently electrical measurements were carried out using HP 4192A impedance analyzer.

Table 2.3: Sintering time and temperature and thickness of different samples prepared.

Composition	Sintering temperature ($^{\circ}\text{C}$)	Sintering time (hrs)	Thickness of the pellet (cm)
Li_2SO_4 (pure)	490	10	0.332
$\text{Li}_2\text{SO}_4+0.02 \text{ FeSO}_4$	490	10	0.332
$\text{Li}_2\text{SO}_4+0.05 \text{ FeSO}_4$	490	10	0.390
$\text{Li}_2\text{SO}_4+0.1 \text{ FeSO}_4$	490	10	0.300
$\text{Li}_2\text{SO}_4+0.2 \text{ FeSO}_4$	490	10	0.308
$\text{Li}_2\text{SO}_4+0.3 \text{ FeSO}_4$	490	10	0.268
$\text{Li}_2\text{SO}_4+0.4 \text{ FeSO}_4$	490	10	0.306
$\text{Li}_2\text{SO}_4+0.5 \text{ FeSO}_4$	490	10	0.400
$\text{Li}_2\text{SO}_4+0.6 \text{ FeSO}_4$	490	10	0.330
$\text{Li}_2\text{SO}_4+0.7 \text{ FeSO}_4$	490	10	0.350
$\text{Li}_2\text{SO}_4+0.8 \text{ FeSO}_4$	490	10	0.400
$\text{Li}_2\text{SO}_4+0.9 \text{ FeSO}_4$	490	10	0.350

CHAPTER 3

Results & Discussion

With the aim of producing a better superionic system, thirteen different compositions of $\text{Li}_2\text{SO}_4 + x \text{FeSO}_4$, $x = 0, 0.02, 0.05, 0.1, 0.2, 0.3, 0.4, 0.5, 0.6, 0.7, 0.8, 0.9$ and 1.0 , were prepared by the conventional solid state reaction route. Also, the traditional technique like melting and quenching was also used to prepare $\text{Li}_2\text{SO}_4 + x \text{FeSO}_4$ samples. Impedance measurements were carried out on these samples in the frequency range 1 kHz to 13 MHz . The X-ray powder diffraction (XRD), BET, Fourier transform infrared spectroscopy (FT-IR) and electrical conductivity results are discussed below.

3.1 X-Ray Diffraction (XRD)

A powerful means of qualitative identification of various crystalline phases is offered by the X-ray diffraction studies. Additionally, the lattice parameter calculations based on the X-ray diffraction results provide a better insight into the structural changes produced in the compound by physical or chemical processes. During the course of present study, X-ray diffraction data are analyzed in greater detail with a view to understand the basic factors responsible for the ionic conductivity in the $\text{Li}_2\text{SO}_4\text{-FeSO}_4$ system.

The X-ray diffraction gives valuable information about the phases present or formation of a compound, if any, as a result of reaction between the constituents. The XRD patterns for $0, 5, 10, 20, 30, 40, 50, 60, 70, 80, 90$ and 100 mol\% FeSO_4 has been recorded using computerized Richeifert powder diffractometer. All these measurements were carried out at room temperature and the results are shown in Figs.3.1-3.3.

No characteristic peaks of FeSO_4 (major peaks at $2\theta = 18.2^\circ$ and 27.5°) are visible in the 5 and 10 mol% FeSO_4 samples while all characteristic peaks of Li_2SO_4 are visible. Therefore it may be inferred from these results that the $\text{Li}_2\text{SO}_4 + x \text{FeSO}_4$ forms solid solution in the composition range $x \leq 0.1$.

The XRD results for 20 mol% FeSO_4 composition is shown in Fig. 3.2B. It is noticed that some of the peaks have grown up in comparison to those of 5 and 10 mol% FeSO_4 . For samples in the composition range $0.2 \leq x \leq 0.7$, the XRD peaks corresponding to both FeSO_4 and Li_2SO_4 are present indicating that these samples are two-phase mixtures. For samples containing 80 and 90 mol% FeSO_4 , the XRD peaks corresponding to Li_2SO_4 almost disappear completely which may suggest partial or total dissolution of Li_2SO_4 in FeSO_4 . Unfortunately, our DTA/DSC facility is not available and hence these results could not be confirmed.

3.1.1 Crystallite Size Determination

The crystallite size was analyzed using Peak Fit v(4) software, which accurately calculates FWHM (full width at half maximum) at 2θ . The standard sample used was that of silicon. The crystallite size was calculated using Debye-Scherrer formula [40]

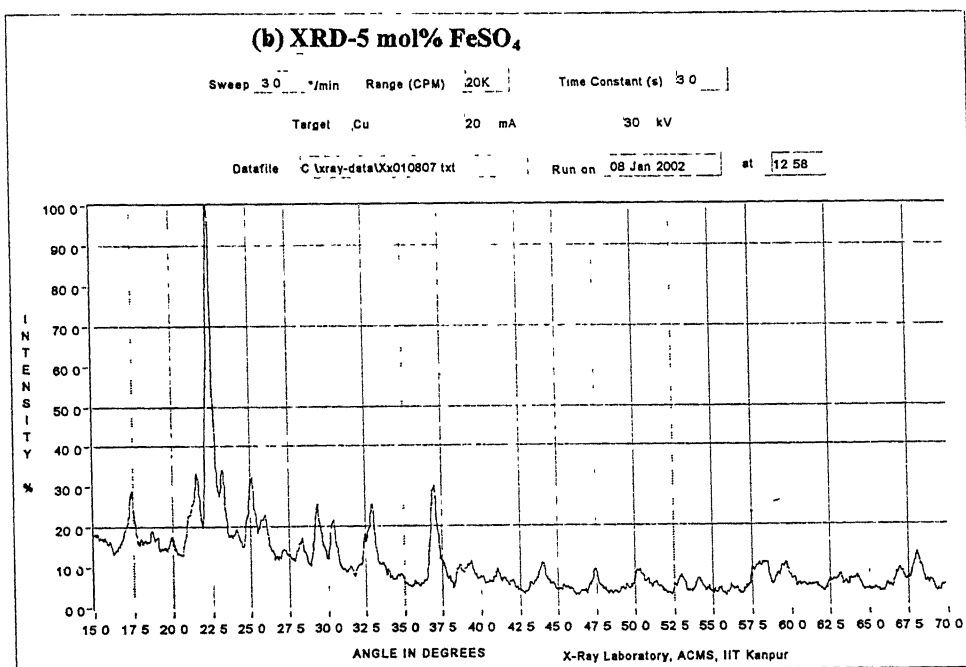
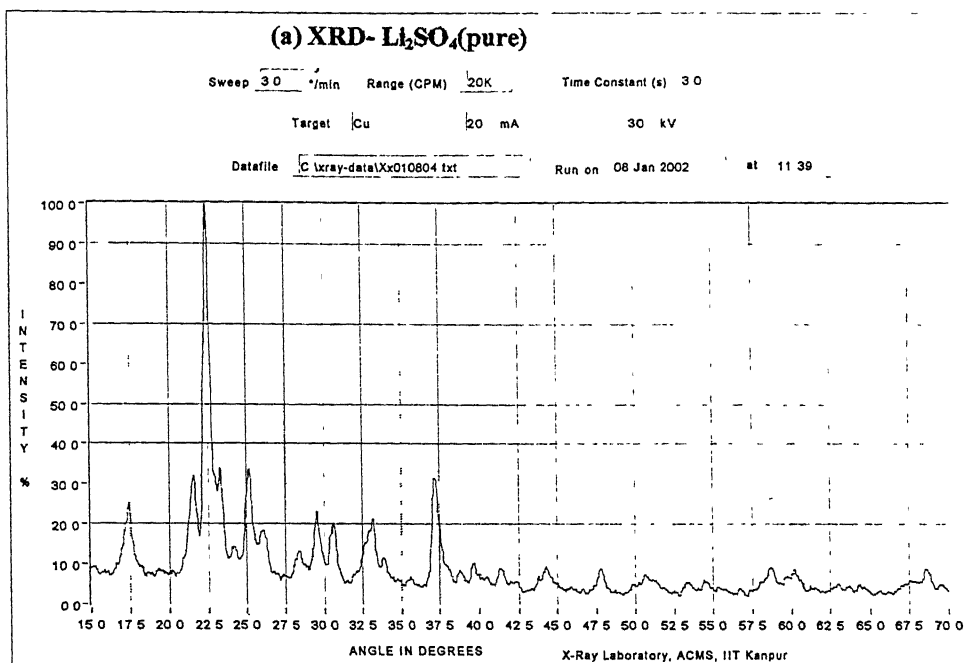


Fig. 3.1: XRD patterns for the pure Li_2SO_4 and $\text{Li}_2\text{SO}_4 + 5 \text{ m/o } \text{FeSO}_4$ samples

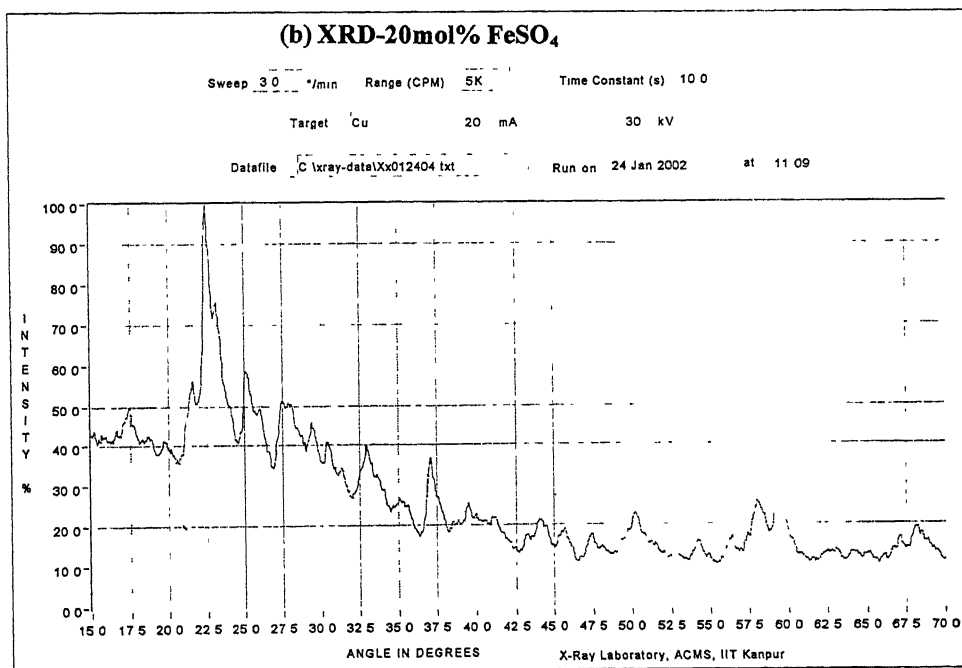
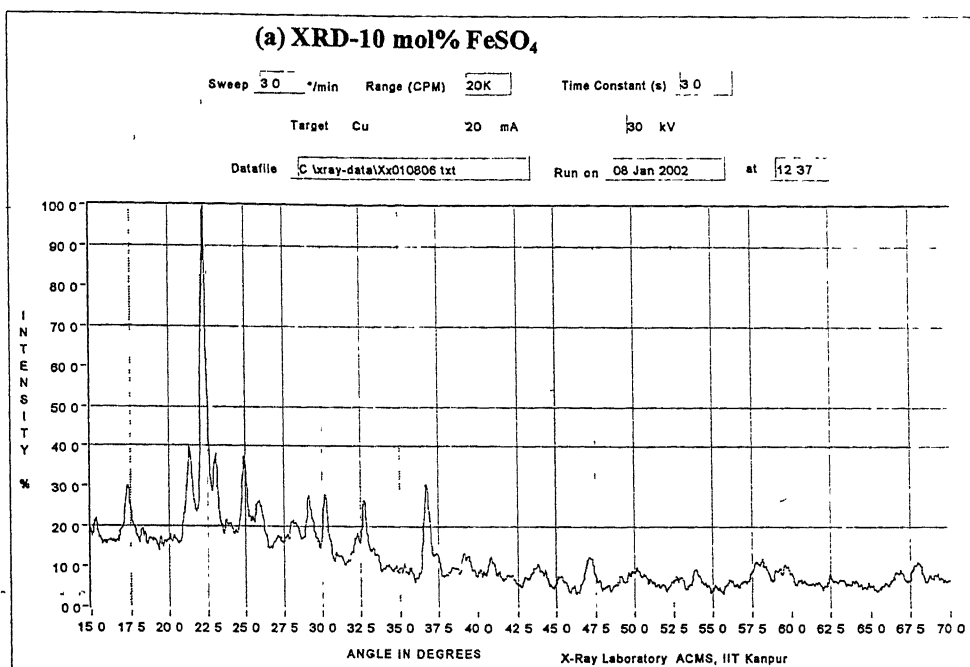


Fig. 3.2: XRD patterns for Li₂SO₄ + 10 m/o FeSO₄ and Li₂SO₄ + 20 m/o FeSO₄ samples

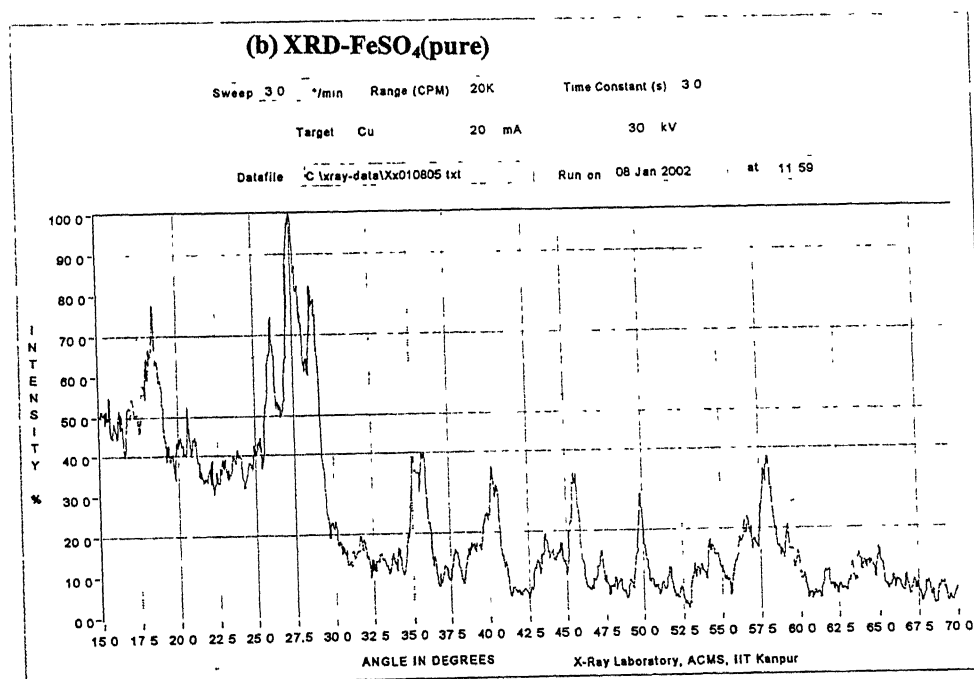
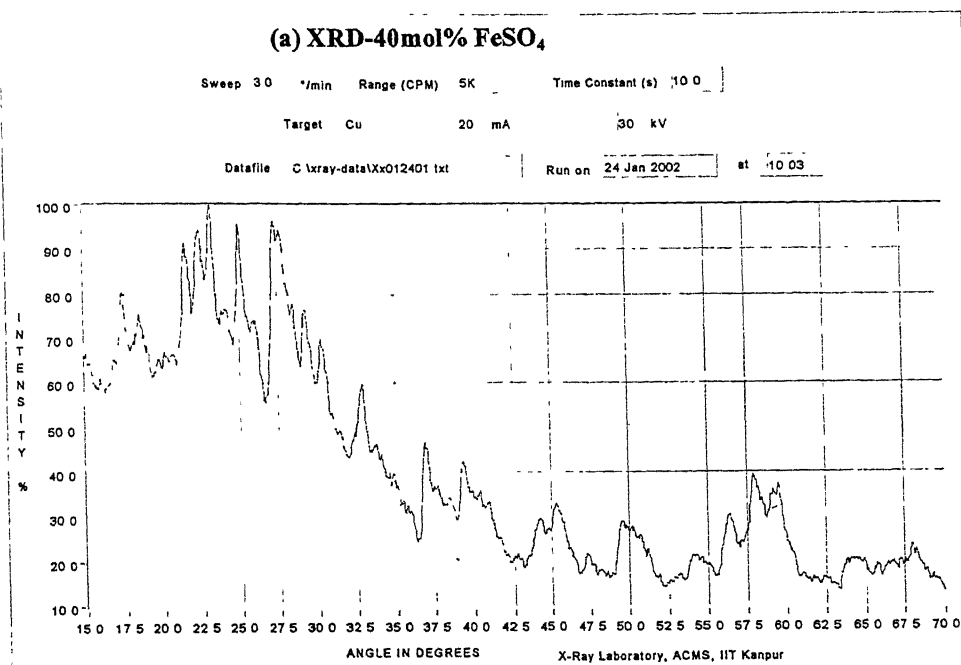


Fig. 3.3: XRD patterns for Li₂SO₄+ 40 m/o FeSO₄ and pure FeSO₄ samples

$$t = \frac{0.9\lambda}{B \cos \theta} \quad (3.1)$$

where λ is the wavelength of the X-ray ($\text{CuK}\alpha$) used which is equal to 1.5404\AA , B is the full width at half maximum after correction from standard sample and θ is the angle at which the peak corresponds to.

$$B = \sqrt{B_m^2 - B_s^2}$$

where B_m is the FWHM of the sample whose crystallite size to be analyzed and B_s is the FWHM of the standard sample (in this case silicon). Each of them are in radians.

Crystallite size has been calculated for two samples, pure Li_2SO_4 and $\text{Li}_2\text{SO}_4 + 10 \text{ m/o FeSO}_4$. The various parameters involved are given in Table 3.1.

Table 3.1: Calculation of crystallite size

Sample ID	B_m (Degrees)	B_s (Degrees)	2θ (Degrees)	Particle size t (nm)
Li_2SO_4	0.83	0.57	25.30	13
$\text{Li}_2\text{SO}_4 + 10$ m/o FeSO_4	0.55	0.54	30.20	60

3.2 BET Measurements

BET measurements have also been used to determine the specific surface area. For this, the samples were prepared by grinding the mixture thoroughly in an agate mortar. The surface area is analyzed by the Coulter SA3100 analyzer, which is based on gas sorption method. The gas used for this purpose was nitrogen. The various parameters involved in BET measurements are listed below in Table 3.2.

Table 3.2: Various quantities involved in BET measurements

Sample ID	Sample wt. (gm)	Elapsed time (min)	Outgas time (min)	Outgas temp. (°C)
Li ₂ SO ₄ + 20 m/o FeSO ₄	0.2987	22	30	120
Li ₂ SO ₄ + 30 m/o FeSO ₄	0.3346	21	30	120

Table 3.3: Specific surface area of two different samples

Sample ID	Specific surface area (m ² /g)	Correlation constant
Li ₂ SO ₄ + 20 m/o FeSO ₄	2.05	0.997
Li ₂ SO ₄ +30 m/o FeSO ₄	3.46	0.999

The low value of specific surface area in all these cases indicates that surface contact may be very poor and this affects the ionic conductivity results. A higher surface area indicates more number of grains in unit gram of the sample. Thus more grain boundaries and hence the path for the migration of ions also increases and hence conductivity. This is attributed to the high conductivity showed by the sample 30 mol% FeSO₄ compared to 20 mol% FeSO₄.

3.3 Fourier Transform Infrared Spectroscopy (FT-IR)

The Fourier transform infrared spectroscopy studies were carried out with a spectrometer model Vector-22(Bruker) in the range 400-4000cm⁻¹. Measurements were made on amorphous material dispersed in KBr in the

ratio 1:30. The resolution of the monochromator is 4 cm⁻¹. Pure Li₂SO₄ and Li₂SO₄ doped with 20, 30 and 40 m/o[mol%] FeSO₄ were analyzed using FT-IR. The FT-IR spectra of these samples are shown in Figs.3.4 and 3.5.

The frequencies corresponding to SO₄²⁻ are given in Table 3.4.

Table 3.4: The observed wave numbers for SO₄²⁻ from FT-IR spectra

Wave number (cm ⁻¹)	Li ₂ SO ₄ (pure)	Li ₂ SO ₄ + 20 m/o FeSO ₄	Li ₂ SO ₄ + 30 m/o FeSO ₄	Li ₂ SO ₄ + 40 m/o FeSO ₄
v ₁ (medium)	640	641	641	640
v ₂ (strong)	1168	1173	1172	1177

Energy considerations (mainly electrostatic and thermodynamic) suggest the splitting of degenerate modes which depends on cations; it increases with increase in ionic radii, ionic polarizability and cation oxygen distance for isomorphous sulphates. As seen in the Figs. 3.4 and 3.5, no other additional frequencies than those corresponding to Li₂SO₄ are present. This rules out the possibility of precipitation or formation of intermediate phase. These results strongly support the XRD results discussed earlier and confirm the solid solution limits.

This study has demonstrated the influence of lattice distortion on the environment of SO₄²⁻ which leads to shift in vibrational frequencies. The appearance of some modified peaks is thus, attributed to change in S-O

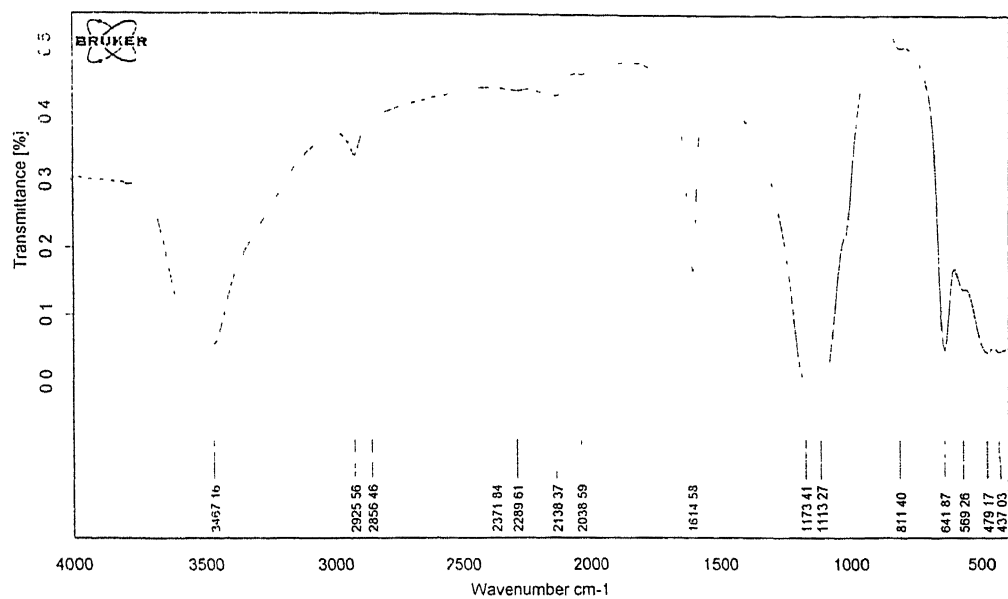
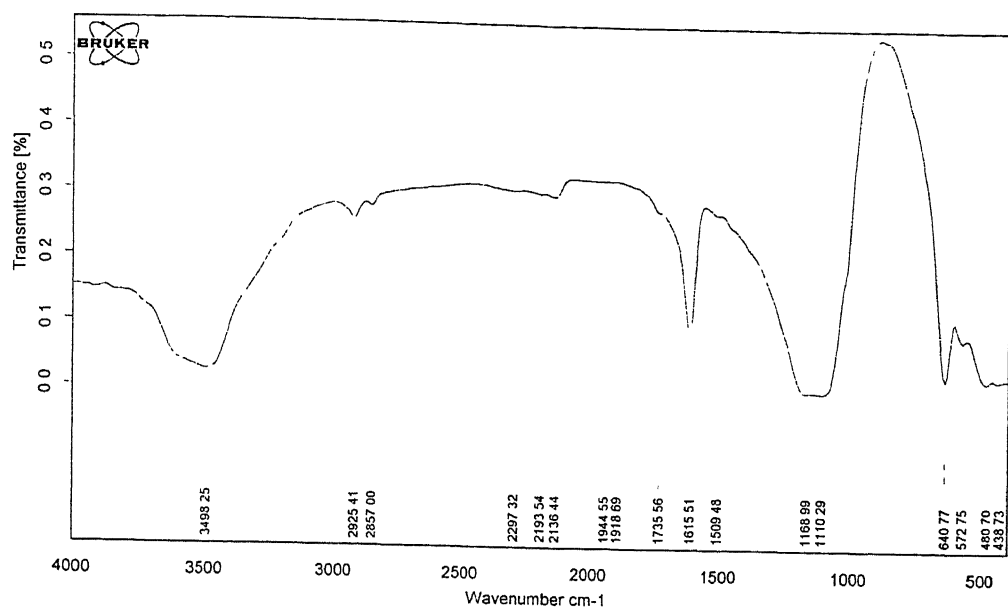


Fig.3.4: FT-IR spectra of pure Li_2SO_4 and $\text{Li}_2\text{SO}_4 + 20 \text{ m/o FeSO}_4$ samples

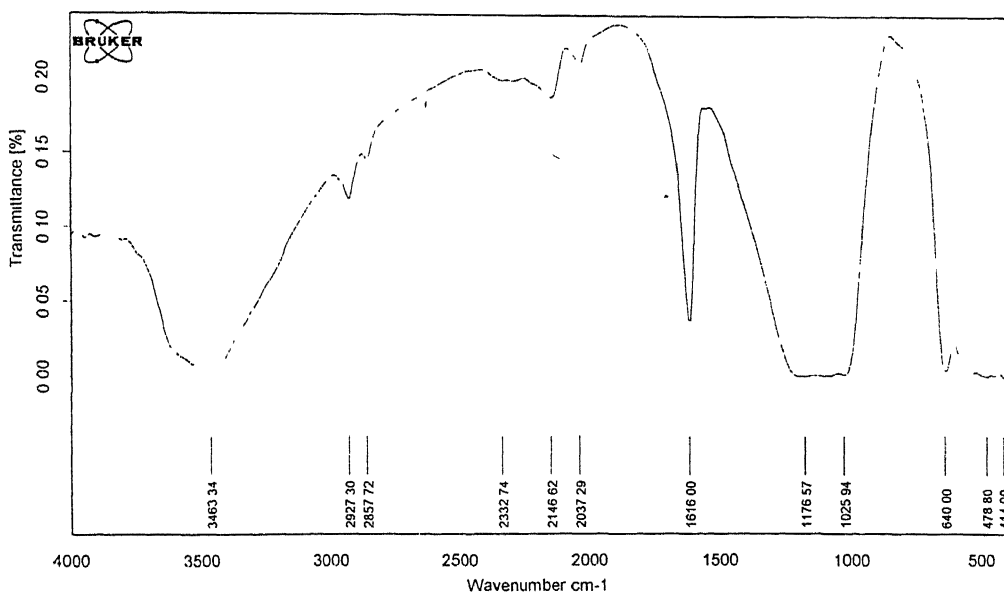
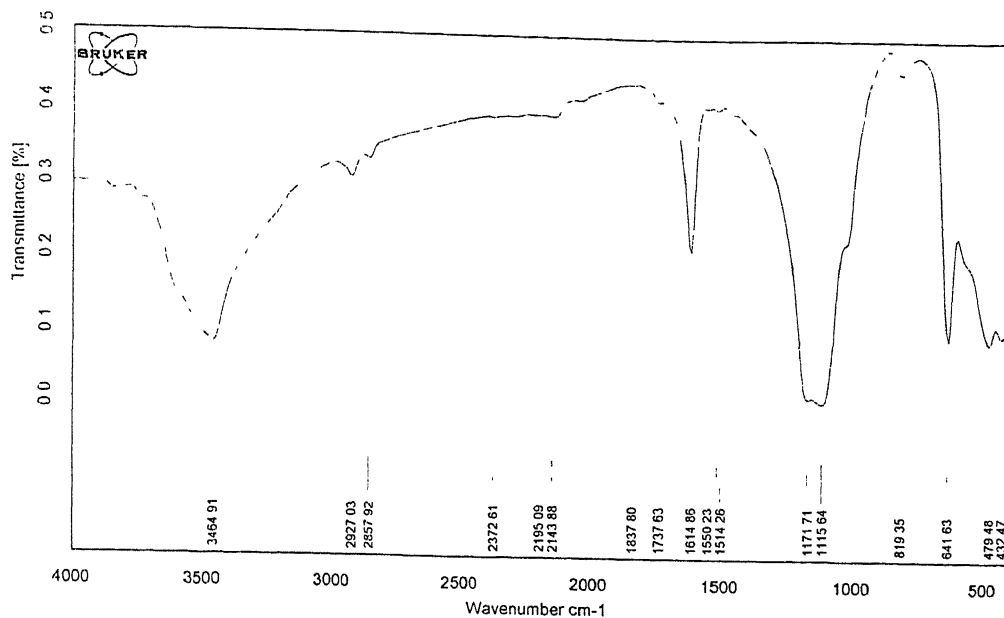


Fig.3.5: FT-IR spectra of $\text{Li}_2\text{SO}_4 + 30 \text{ m/o FeSO}_4$ and $\text{Li}_2\text{SO}_4 + 40 \text{ m/o FeSO}_4$ samples

distance. These modifications support the concept of lattice distortion, which influences the mobility of the ions in the lattice.

3.4 Impedance analysis

The complex impedance analysis basically gives the different interfacial components present in the conductivity experiments. It can be pure resistance, pure capacitance or a combination of both. The presence of these elements is determined by plotting a graph between the imaginary part of the impedance ($Z\sin\theta$) along the y-axis and the real part ($Z\cos\theta$) along the x-axis. The different shapes of the curve is an indication of the presence of various elements.

Figs.3.6a and b show the impedance plots at different temperatures for the pure Li_2SO_4 and $\text{Li}_2\text{SO}_4 + 10 \text{ m/o FeSO}_4$ samples, showing reasonably good semicircles, within the experimental errors. As shown earlier in Chapter two,

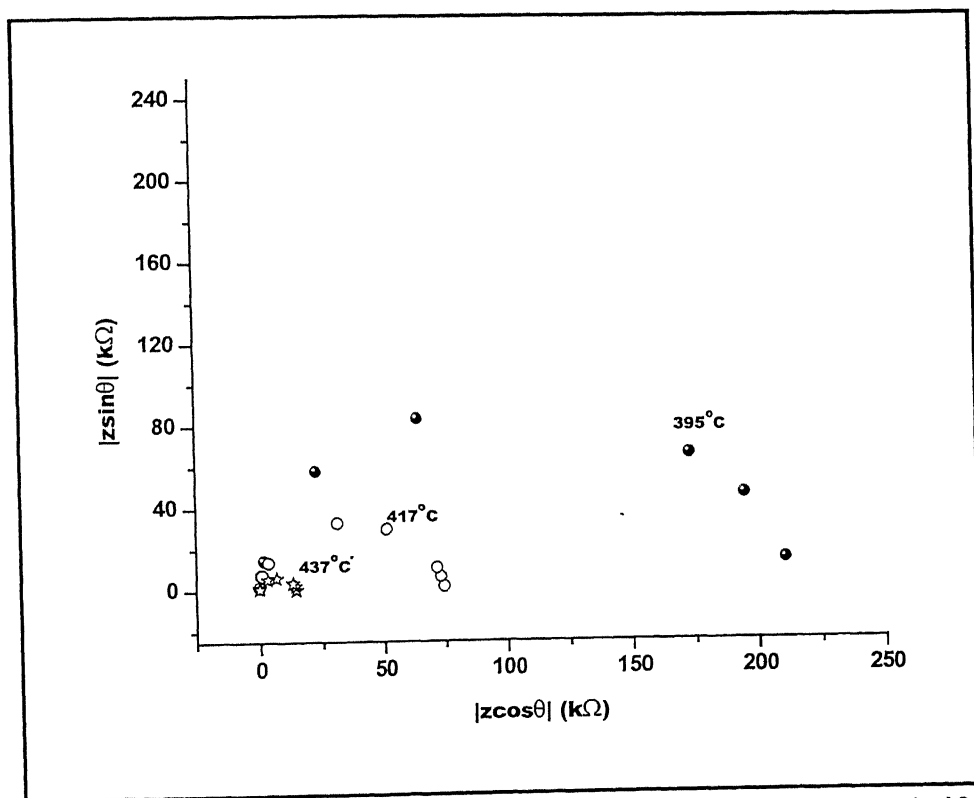


Fig.3.6a: Impedance plot for pure Li_2SO_4 at 395, 417 and 437°C

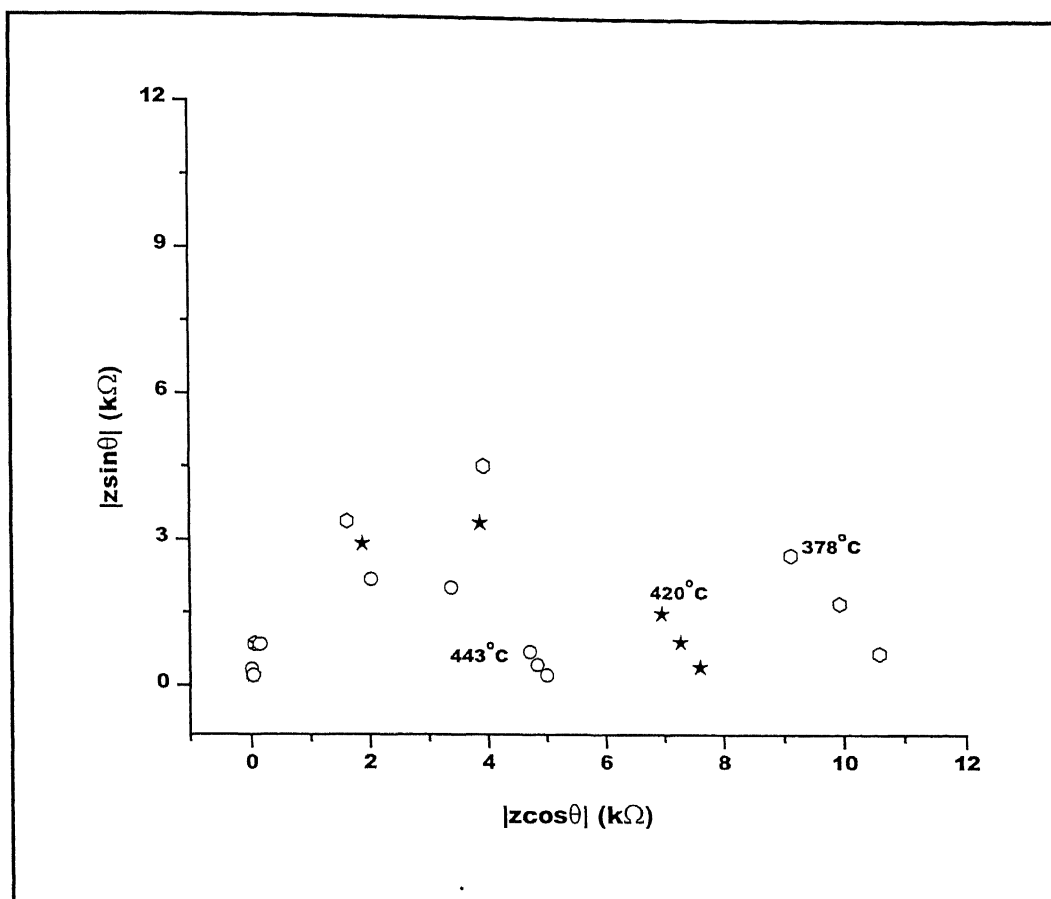


Fig.3.6b: Impedance plot for $\text{Li}_2\text{SO}_4+10\text{m/oFeSO}_4$ at 378, 420 and 443°C

it is a result of the parallel mode of combination of capacitor and resistor. The diameter of the circle gives the dc resistance (R_{dc}) of the sample at that particular temperature.

As clearly visible in Fig.3.6a and b, on increasing the temperature, the diameter of the semicircle decreases, which indicates the dc resistance (R_{dc}) of the sample also decreases. This is as expected because the ionic conductivity of crystalline solids generally increases with temperature and $\sigma \cdot T$ obeys the Arrhenius law. At higher temperatures, the carriers have enough

energy to overcome the energy barrier created by the field of ions, and hence more number of carriers contributes towards mobility, and hence conductivity.

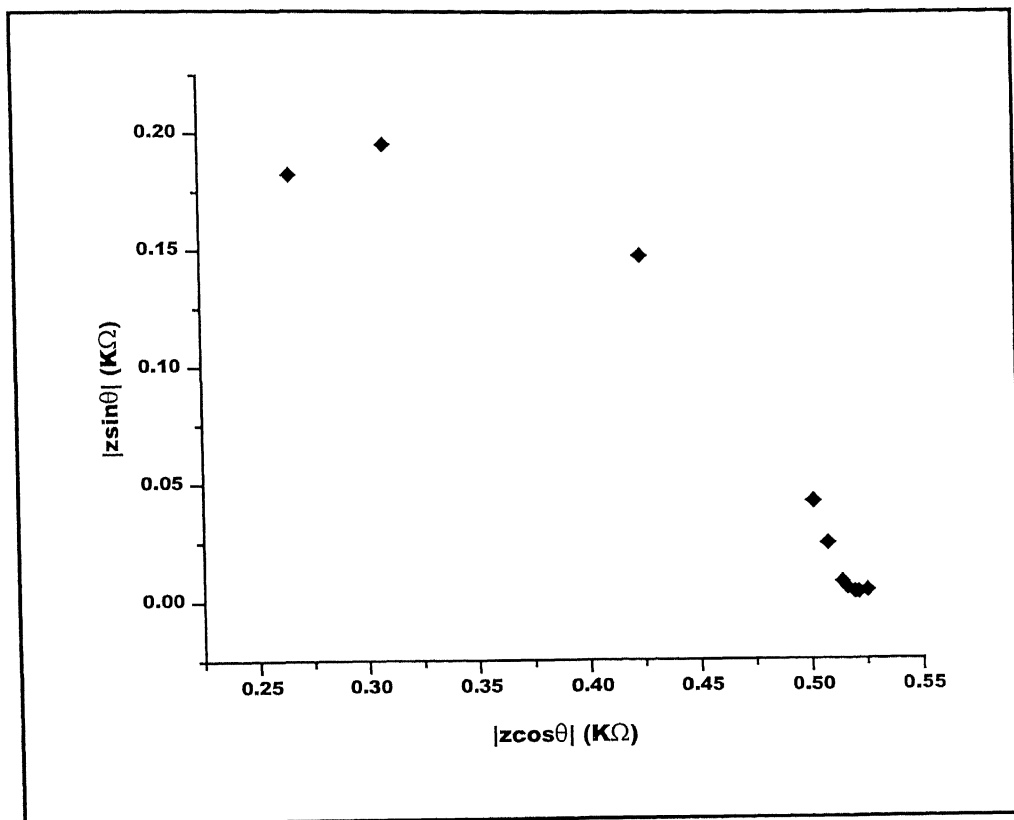


Fig.3.7: Impedance plot for $\text{Li}_2\text{SO}_4 + 60 \text{ m/o FeSO}_4$ at 512°C .

The impedance plot shown in Fig.3.7 for 60 m/o FeSO_4 sample exhibits a small line in addition to the semicircle, at the low frequency end. This is due to the interfacial capacitance at the electrode/electrolyte interface. This gives some idea about the smoothness of the interface.

3.5 DC conductivity

The electrical conductivity of the low temperature phase ($T < 575^\circ\text{C}$) of lithium sulphate, i.e., $\beta\text{-Li}_2\text{SO}_4$, as well as high temperature phase ($T >$

पुस्तकालय काशीनाथ कलकर पुस्तकालय
आर्य समाज प्रौद्योगिकी संस्थान काशी
141851
अवधि क्र० A

575⁰C) i.e., α -Li₂SO₄, was measured using a HP 4192A impedance analyzer. Samples were prepared in two different ways, mechanical mixing and melt-quenching. Of these the samples obtained by mechanical mixing were better and accordingly we concentrated on mechanically prepared samples. A comparison of the conductivities of the samples prepared by different routes for two different samples (30 and 40 mol% FeSO₄) is shown in Figs.3.8 and 3.9. Surprisingly, the conductivity of mechanically mixed sample is higher than that of melt-quenched sample. The enhancement in conductivity may be due to the formation of mechanical bonds rather than chemical bonds. It may be attributed to the fact that the addition of FeSO₄, which acts as a dispersant, induces changes in the charged defect concentrations in the surrounding matrix so that the conductivity of the host phase (i.e. Li₂SO₄) is enhanced. Or that each particle acts as a carrier of some chemical species (e.g. water molecules), which interacts with the host to form a high conductivity coating surrounding each inclusion. This may be the reason why mechanically prepared samples are highly conducting compared to melt-quenched samples.

3.5.1 Conventional Samples

The variation of electrical conductivity (σ) with inverse of absolute temperature is shown in Fig.3.10 for pure Li₂SO₄. The observed behavior of conductivity –inverse temperature (σ vs. $1/T$) is in accordance with theory of ionic transport in solids, namely that the conductivity varies exponentially with $1/T$ as given in eqn.(1.9), rewritten for ready reference.

$$\sigma = n(T)q\mu(T) = \sigma_0 \exp[-E_a/(kT)] \quad (3.1)$$

Where $n(T)$ is the concentration of mobile defects, e their charge, $\mu(T)$ their mobility, σ_0 the pre-exponential factor, E_a is the overall activation energy for conduction, k the Boltzmann's constant and T the temperature.

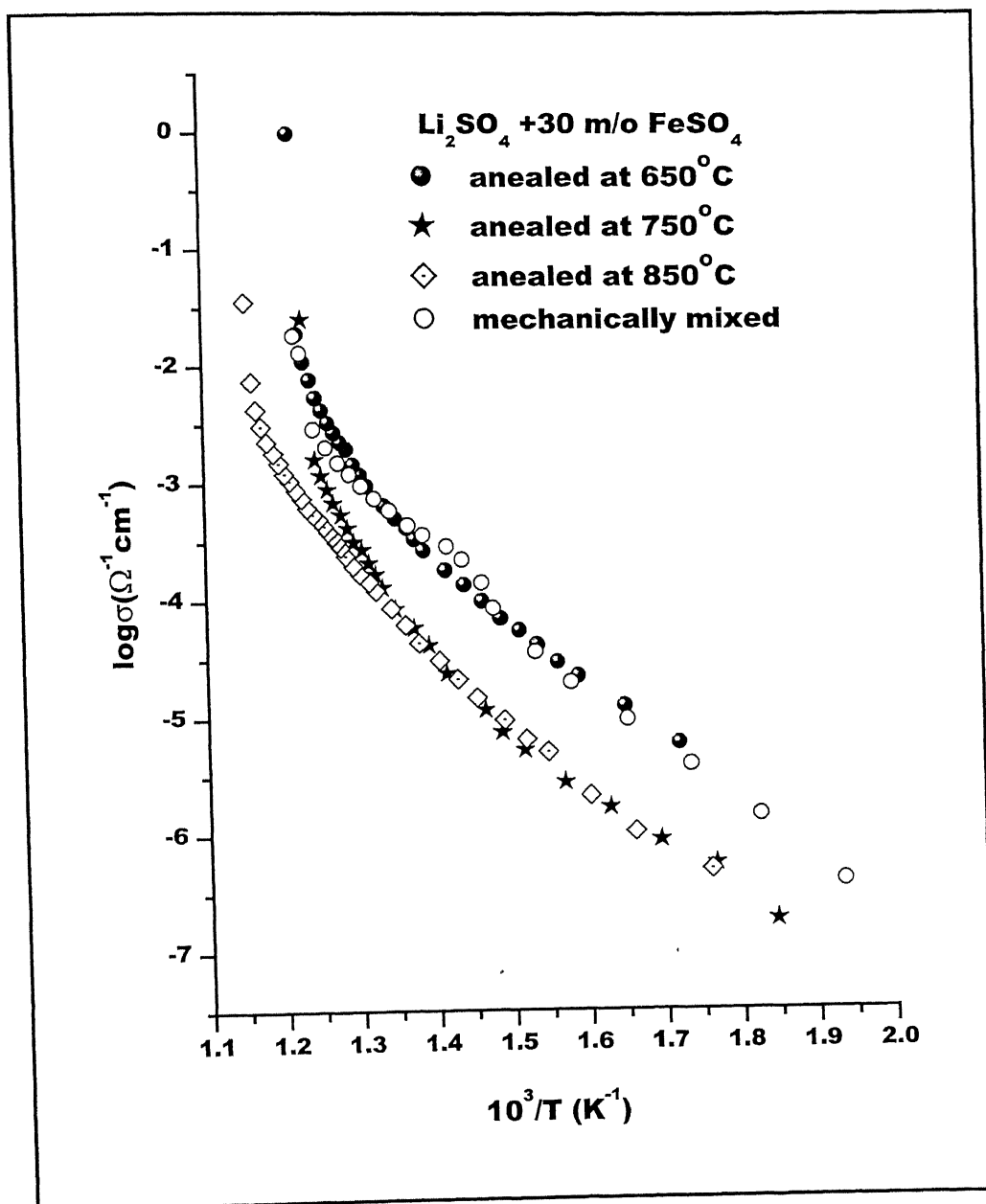


Fig.3.8: DC conductivity of Li₂SO₄ + 30 m/o FeSO₄ prepared by different routes

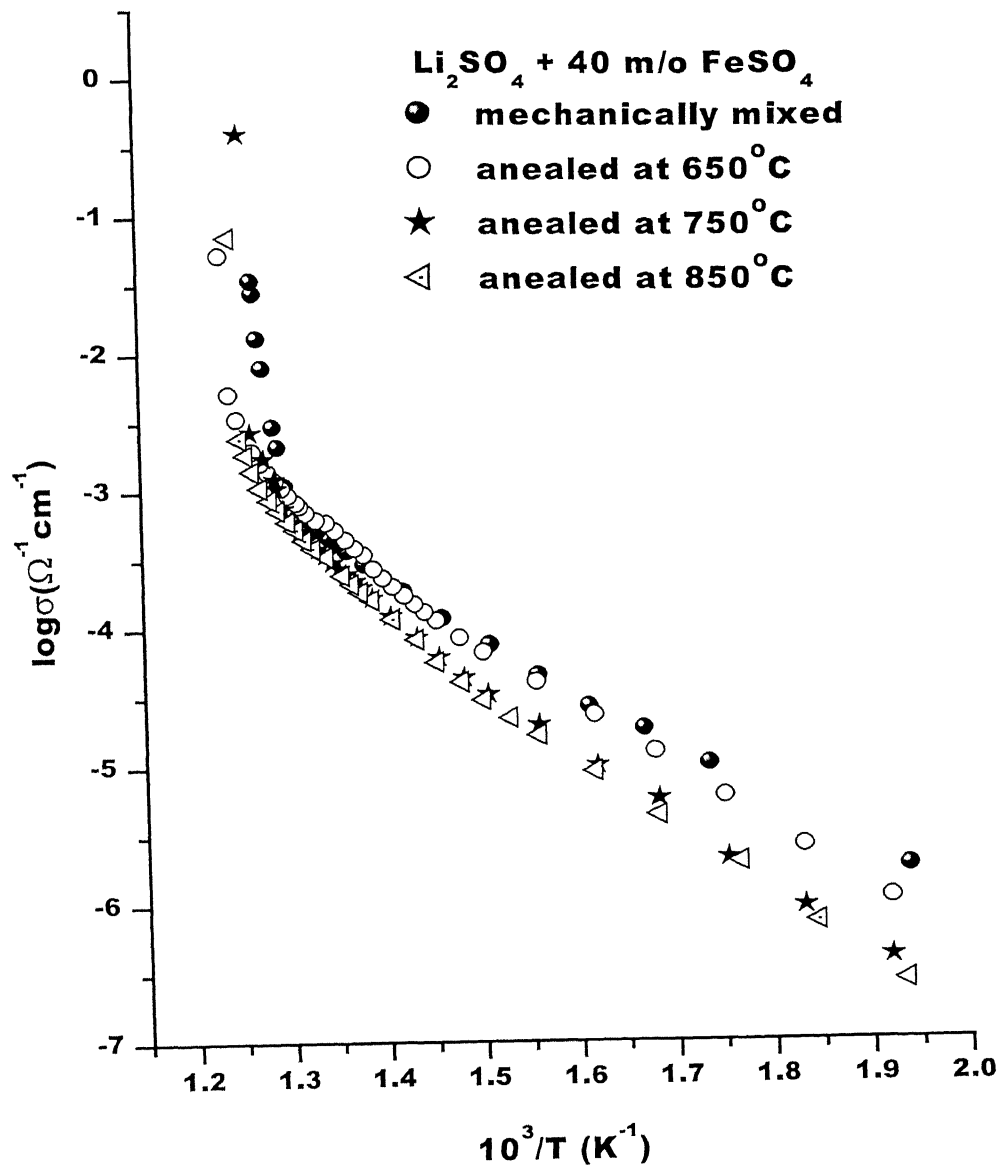


Fig. 3.9: DC conductivity of Li₂SO₄ + 40 m/o FeSO₄ prepared by different routes

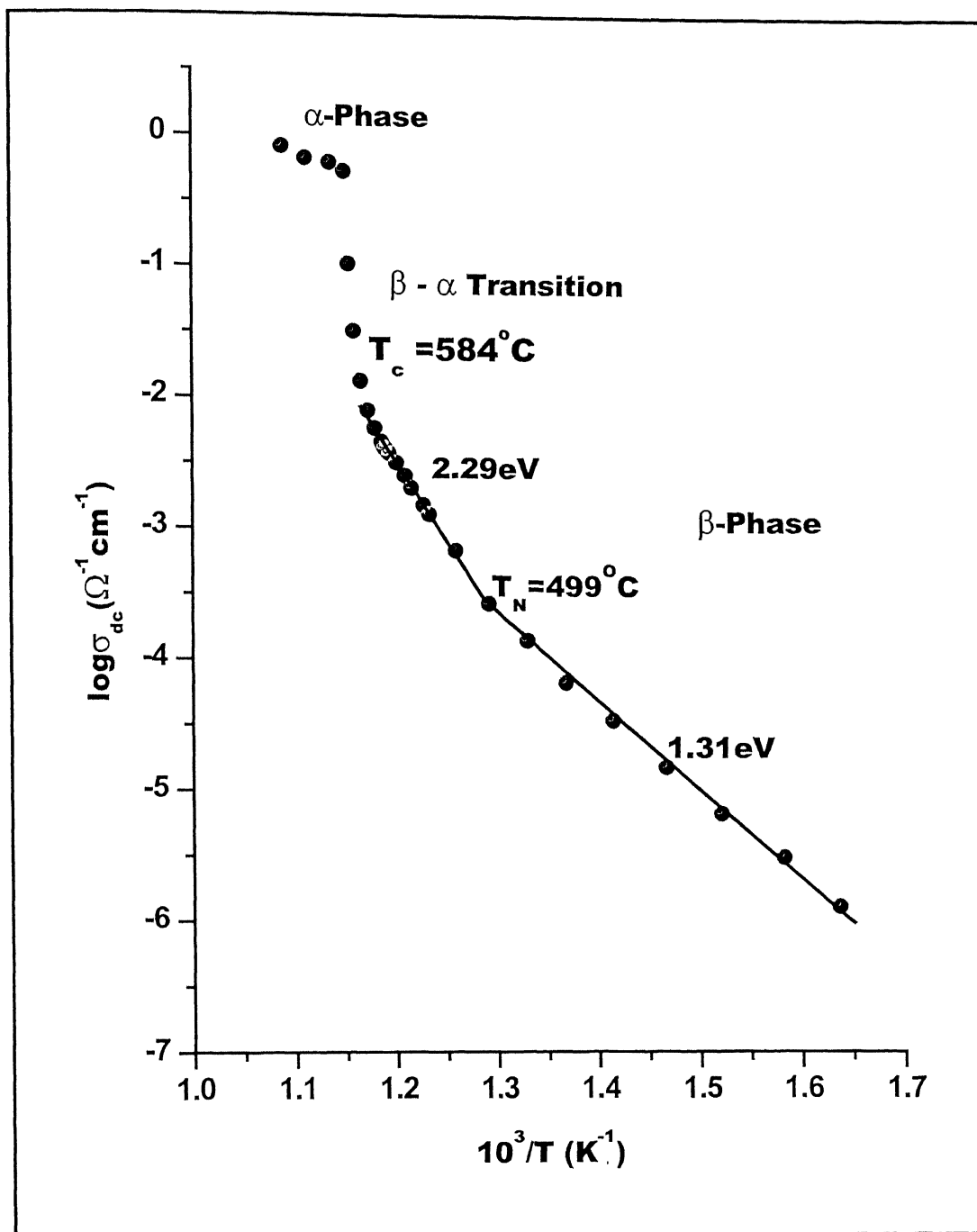


Fig. 3.10: DC conductivity of pure Li_2SO_4

Thus according to Eqn.(3.1), $\log\sigma$ should vary linearly with $1/T$ and the slope of the linear plot should yield the activation energy

$$E_a = -2.3026 k \times \text{slope (of } \log\sigma \text{ vs. } 1/T) \quad (3.2)$$

The intercept of $\log\sigma$ vs. $10^3/T$ plot on $\log\sigma$ -axis gives the pre-exponential factor σ_0 . These two parameters, viz. σ_0 and E_a , are used to characterize the bulk (macroscopic) conduction properties of solid electrolytes. The calculated values of σ_0 and E_a from the linear plot of $\log\sigma$ as a function of inverse temperature (Fig.3.10) for $\beta\text{-Li}_2\text{SO}_4$ is given in Table 3.5 which also includes the σ_0 and E_a values for other compositions studied in this work.

Here we should point out that theoretically it is $\log(\sigma T)$, which varies exponentially with $1/T$, and thus $\log(\sigma T)$ vs. $1/T$ should be plotted and used for the calculation of E_a . However, in $\log(\sigma T) = \log\sigma + \log T$, the variation of $\log\sigma$ is far greater than that of $\log T$, and therefore negligence of the term $\log T$ hardly makes any difference. It can be illustrated from the following example: suppose σ varies from 10^{-8} to $10^{-2} \text{ ohm}^{-1}\text{cm}^{-1}$ corresponding to a change in T from 300 to 800K. Thus while $\log\sigma$ changes by 6, $\log T$ changes only by 0.42 (or $\sim 7\%$). Thus the activation energy (E_a) extracted from $\log(\sigma T)$ vs. $1/T$ plots would be generally higher by a few percent than E_a (obtained from $\log(\sigma)$ vs. $1/T$ plot). However the latter is preferred because it is more convenient to plot and compare with other studies.

Table 3.5: Ionic transport parameters for Li₂SO₄-FeSO₄ system

Material Composition	σ at T ⁰ C ($\Omega^{-1}\text{cm}^{-1}$)	E _a (eV)	T-range (⁰ C)	σ_0 ($\Omega^{-1}\text{cm}^{-1}$)
Pure Li ₂ SO ₄	1.38x10 ⁻⁴ at 479 7.81x10 ⁻³ at 580	1.60 2.29	347-499 499-584	8.20x10 ⁴ 2.19x10 ⁶
Li ₂ SO ₄ + 2 m/o FeSO ₄	1.92x10 ⁻⁵ at 416 9.34x10 ⁻³ at 578	0.99 1.78	280-416 416-581	0.64 3.18x10 ⁸
Li ₂ SO ₄ + 5 m/o FeSO ₄	1.10x10 ⁻⁴ at 461 5.24x10 ⁻³ at 563	1.07 1.83	281-466 466-566	2.41x10 ³ 5.51x10 ⁸
Li ₂ SO ₄ + 10 m/o FeSO ₄	3.63x10 ⁻⁵ at 446 2.55x10 ⁻³ at 554	0.93 1.84	303-449 449-560	1.18x10 ² 4.07x10 ⁸
Li ₂ SO ₄ + 20 m/o FeSO ₄	1.92x10 ⁻⁵ at 388 1.44x10 ⁻³ at 533	0.88 1.20	311-390 390-537	97.02 4.52x10 ⁴
Li ₂ SO ₄ + 30 m/o FeSO ₄	2.00x10 ⁻⁵ at 360 2.92x10 ⁻³ at 530	0.82 1.19	244-377 377-534	66.66 8.46x10 ⁴
Li ₂ SO ₄ + 40 m/o FeSO ₄	2.78x10 ⁻⁵ at 347 1.12x10 ⁻³ at 497	0.74 0.93	243-348 348-497	28.44 1.35x10 ³
Li ₂ SO ₄ + 50 m/o FeSO ₄	1.34x10 ⁻⁴ at 405	0.73	227-408	35.47
Li ₂ SO ₄ + 60 m/o FeSO ₄	2.55x10 ⁻⁴ at 447	0.87	238-449	309.64
Li ₂ SO ₄ + 70 m/o FeSO ₄	3.35x10 ⁻⁵ at 334	0.74	200-335	46.09
Li ₂ SO ₄ + 80 m/o FeSO ₄	7.78x10 ⁻⁵ at 345	0.71	185-359	47.41
Li ₂ SO ₄ + 90 m/o FeSO ₄	1.54x10 ⁻⁴ at 340	0.64	185-365	27.84
Pure FeSO ₄	2.44x10 ⁻⁴ at 339	0.62	169-350	30.80

As far as conductivity-temperature behaviour of pure Li_2SO_4 , we find two different regions in $\log\sigma$ vs. $10^3/T$ plot (Fig.3.10) associated with $E_a = 1.31$ eV in the range 347-499°C and 2.29 eV in the range 499-584°C. The low temperature region may be called extrinsic- conduction region in which the conduction occurs through diffusion via lattice (bulk conduction) but the mobile lattice defects are introduced by the presence of accidental (aliovalent) impurities, rather than produced as a result of thermodynamic requirement. This region is therefore impurity-controlled extrinsic-region in which the concentration of mobile defects is independent of temperature and is far more than those produced by thermal activation. Thus the activation energy $E_a = 1.31$ eV may be identified as the activation energy for migration (h_m) alone.

$$\text{i.e. in } \beta\text{-Li}_2\text{SO}_4 \quad E_a = h_m = 1.31\text{eV} \quad (347\text{-}499^\circ\text{C}) \quad (3.3)$$

The high temperature region between 499 and 584°C is the intrinsic region of conduction. In this temperature range the thermally produced defects outnumber those present as a result of aliovalent impurities. Thus overall activation energy contains both terms i.e.,

$$E_a = 1/2h_f + h_m = 2.29 \quad (3.4)$$

From Eqns. (3.3) and (3.4) we get

$$h_f = 1.96\text{eV} \quad (3.5)$$

As such the activation energy for the formation of defects in $\beta\text{-Li}_2\text{SO}_4$ i.e., $h_f = 1.96$ eV sounds reasonable. However, the activation energy for migration $h_m = 1.31$ eV appears somewhat larger [12].

The migration energy in the superionic phase of $\alpha\text{-Li}_2\text{SO}_4$ obtained in the present work is compared with literature data in Table 3.6.

Table 3.6: Energy of migration in α -Li₂SO₄

E_a (eV)	Reference
0.41	42
0.30	43
0.45	44
0.44	45
0.34 ^a	45
0.42	25
0.50	Present work

^a Determined from diffusion measurements.

Thus our present results for both β - and α -Li₂SO₄ are in good agreement with previous measurements (Table 3.6) within the experimental error, except with those of Singh *et al.* [43] and Kvist and Lunden [45].

The present measurement showed that α -Li₂SO₄ has a conductivity of $0.81\Omega^{-1}\text{cm}^{-1}$ at 919 K which may be compared with that obtained by Kvist and Lunden [45]; $\sim 3\Omega^{-1}\text{cm}^{-1}$ close to the melting point (1133 K). The difference between the two results may be due to the following reasons: (1) We are 114 K away from the melting point of Li₂SO₄; (2) different palletizing pressures may yield different conductivities and (3) electrode-electrolyte contact resistance may also affect the conductivity values.

Electrical conduction in the normal conducting phase (β -phase) is mainly caused by Schottky or Frenkel defects. Cation Frenkel defects have been shown to dominate in AgCl, AgBr and AgI [46, 47] and it is thus reasonable to assume that cation Frenkel defects also dominate in the monoclinic phase of Li₂SO₄. The mobility of lithium ions is much larger than the mobility of sulphate ions in Li₂SO₄ and as a first approximation it

may be considered that lithium ions are solely responsible for the ionic conductivity in the normal conducting phase (β -phase) of Li_2SO_4 [25].

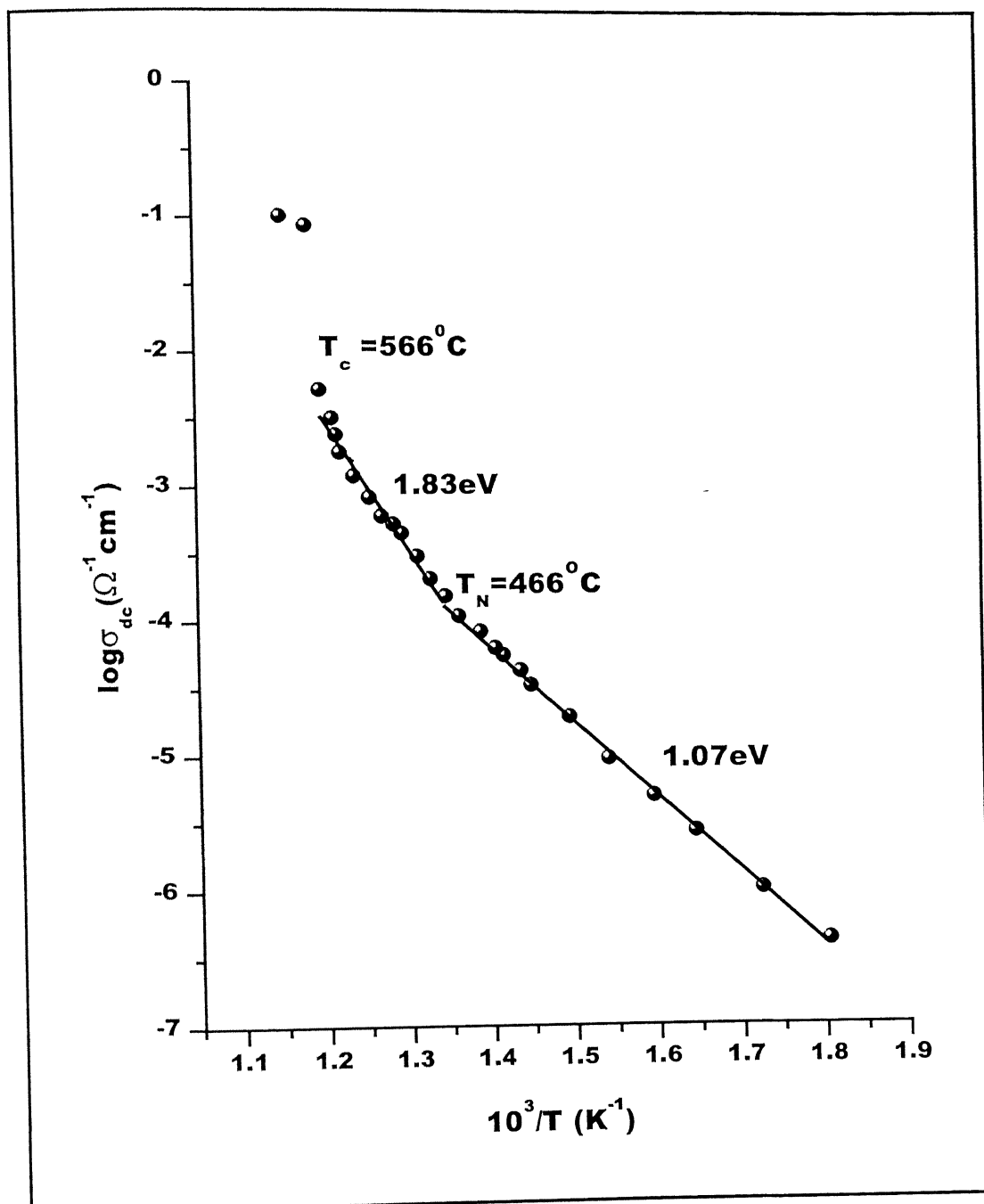


Fig.3.11: DC conductivity of $\text{Li}_2\text{SO}_4 + 5 \text{ m/o FeSO}_4$

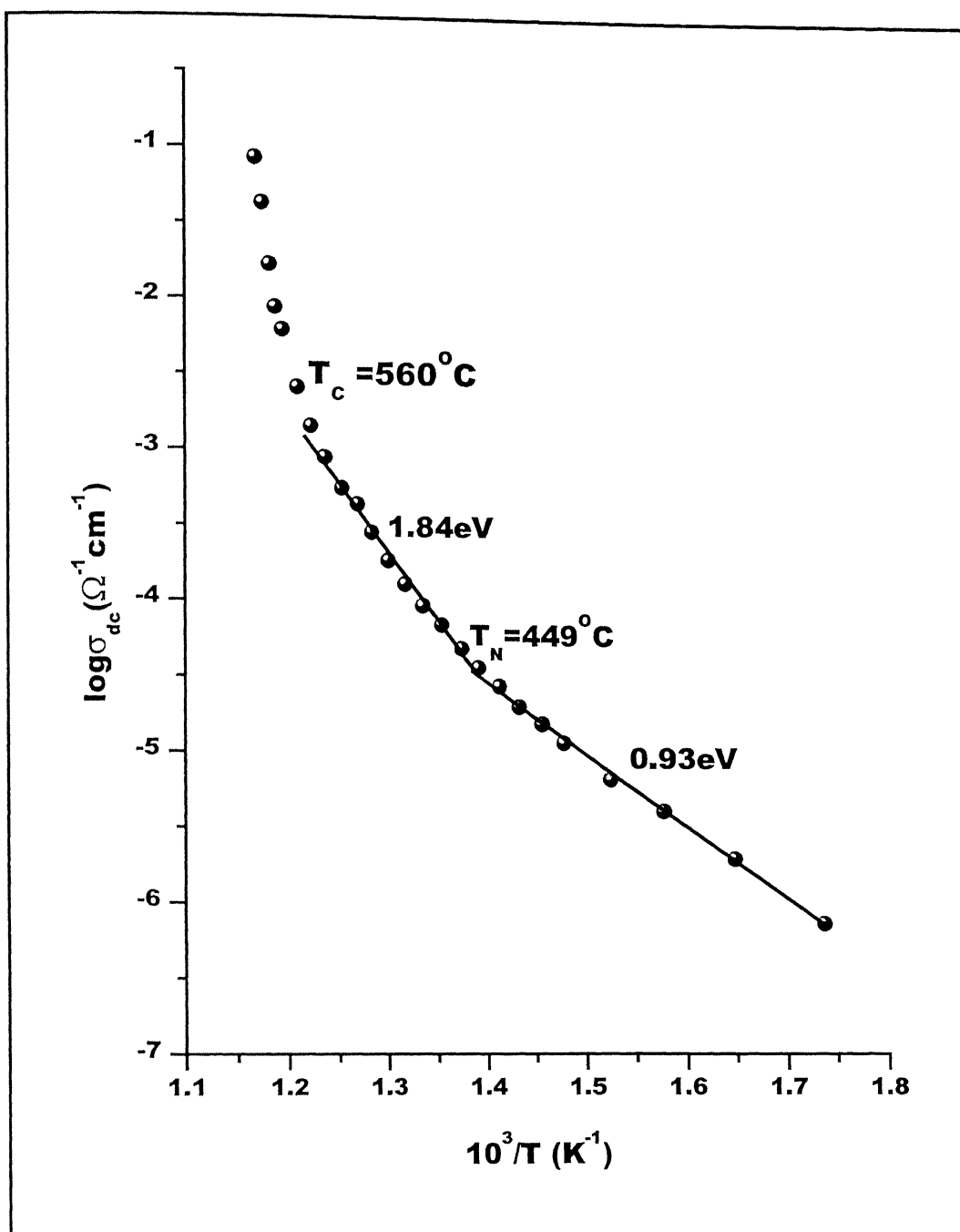


Fig.3.12: DC conductivity of $\text{Li}_2\text{SO}_4 + 10 \text{ m/o FeSO}_4$

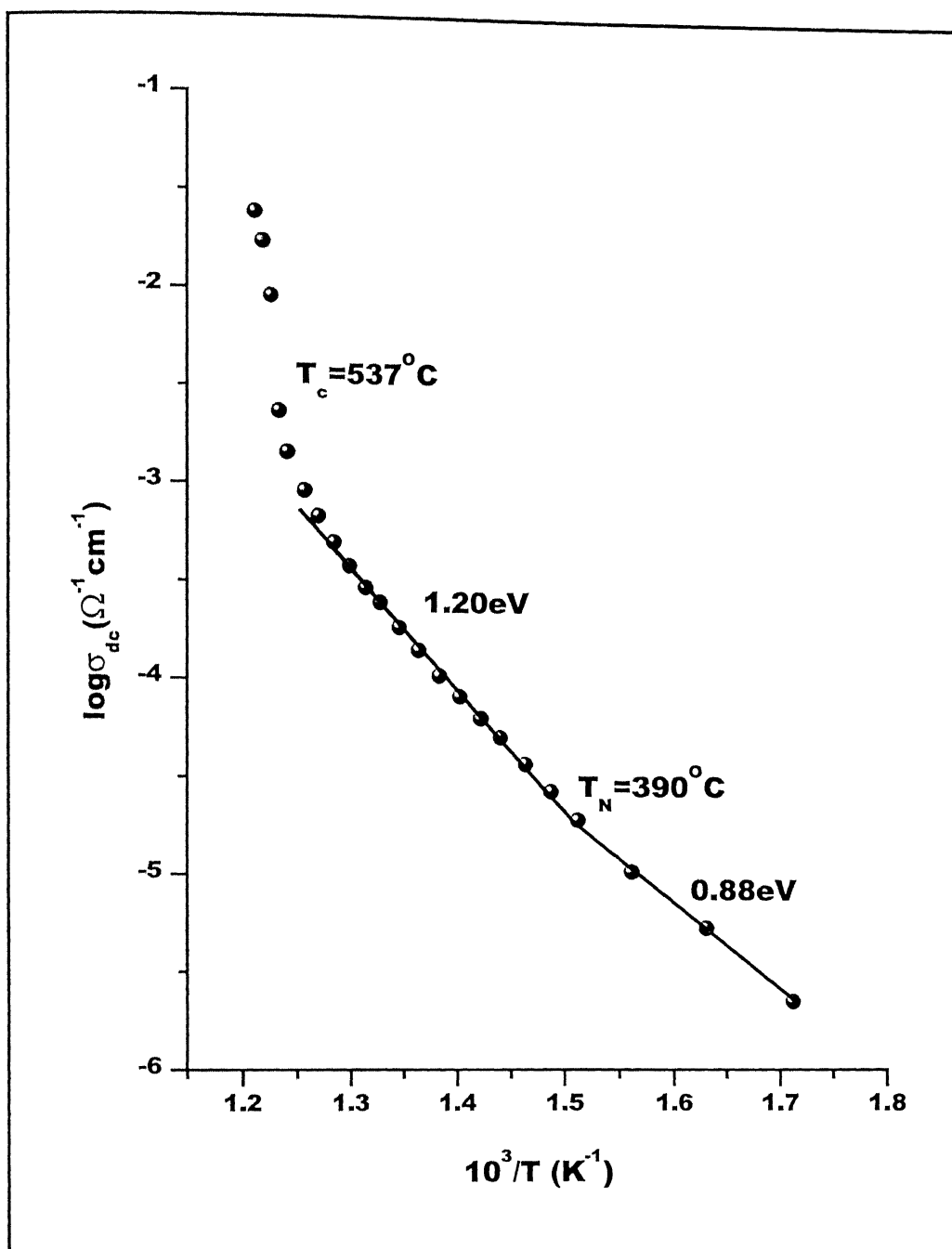


Fig.3.13: DC conductivity of $\text{Li}_2\text{SO}_4 + 20 \text{ m/o FeSO}_4$

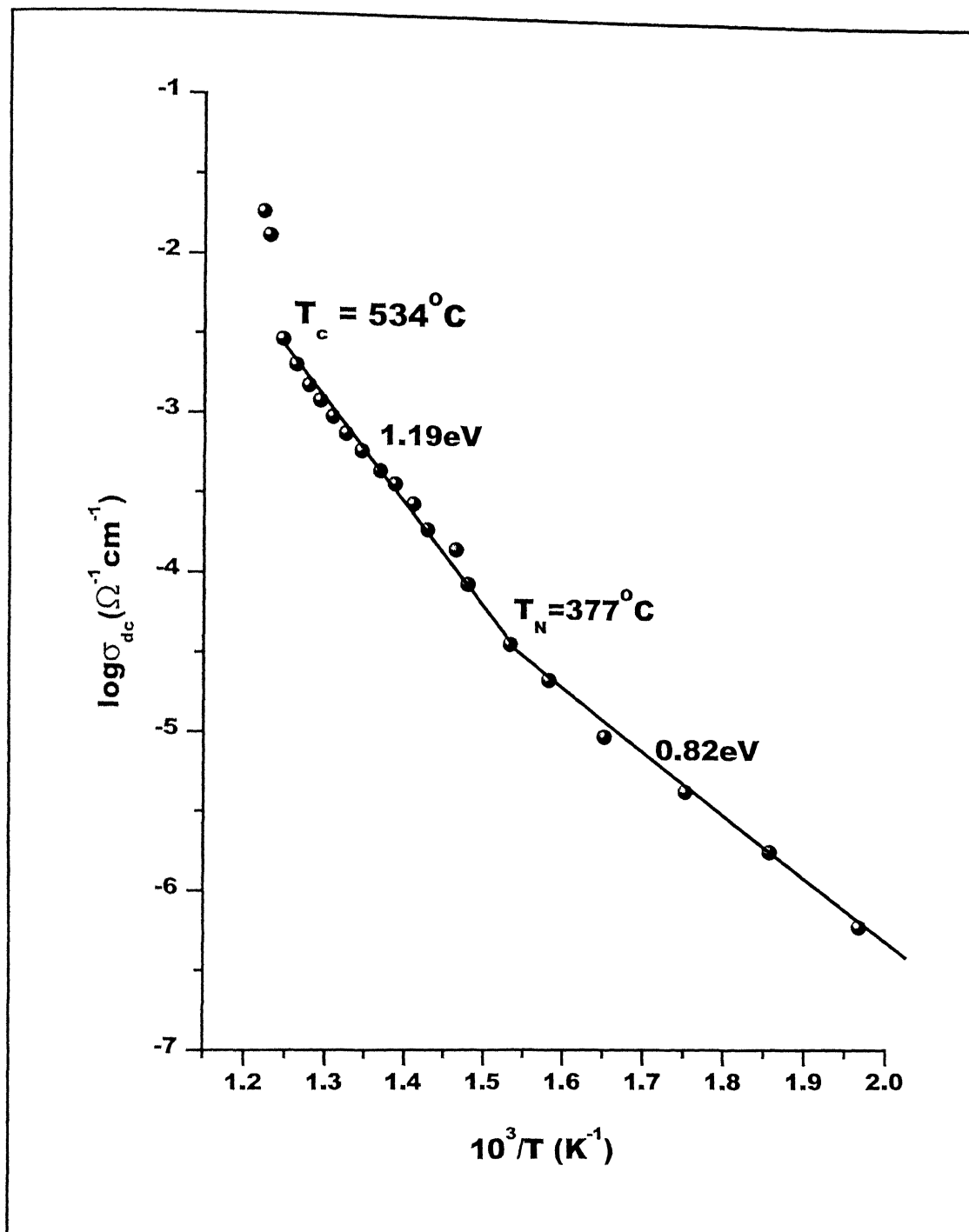


Fig.3.14: DC conductivity of $\text{Li}_2\text{SO}_4 + 30 \text{ m/o FeSO}_4$

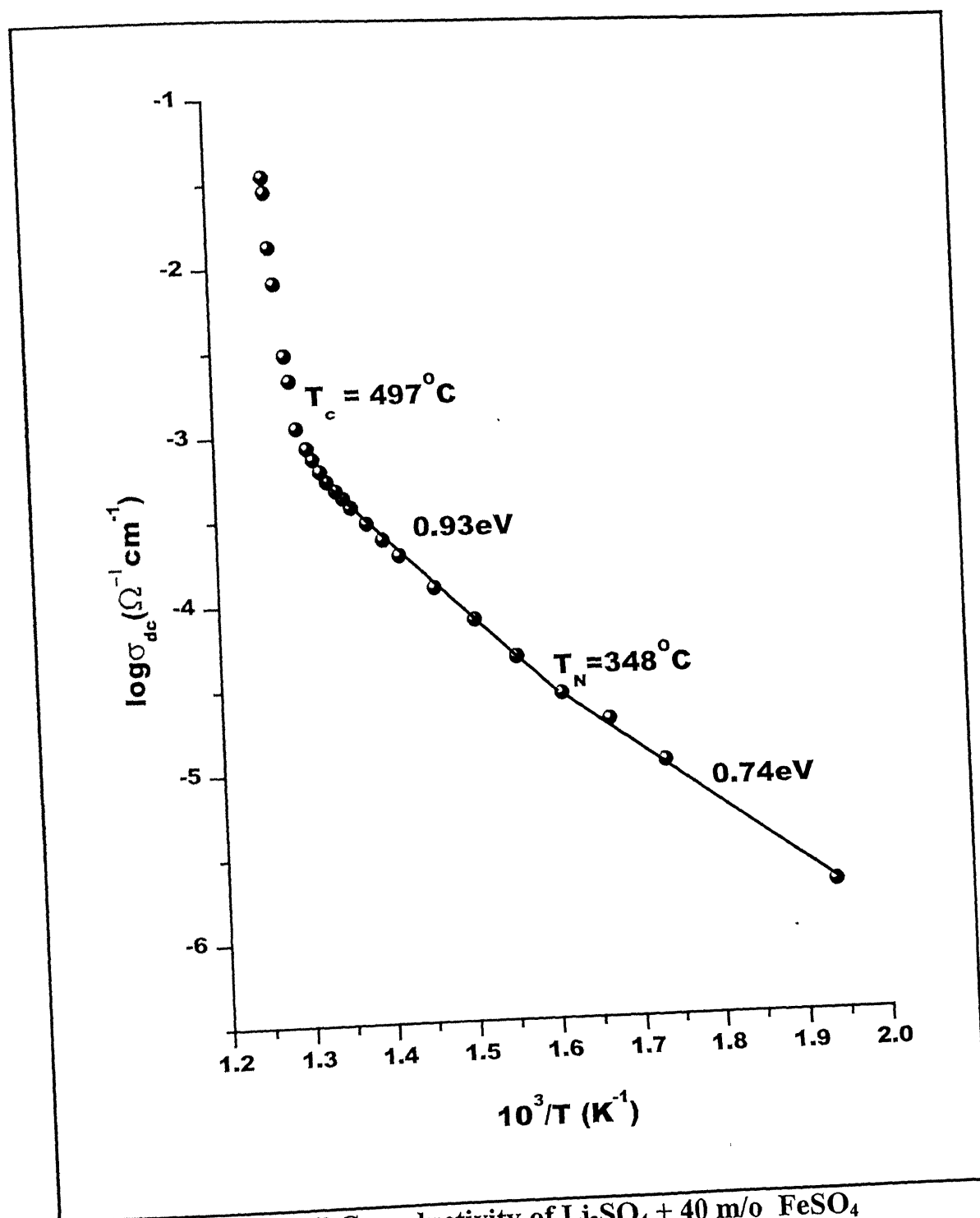


Fig.3.15: DC conductivity of $\text{Li}_2\text{SO}_4 + 40 \text{ m/o FeSO}_4$

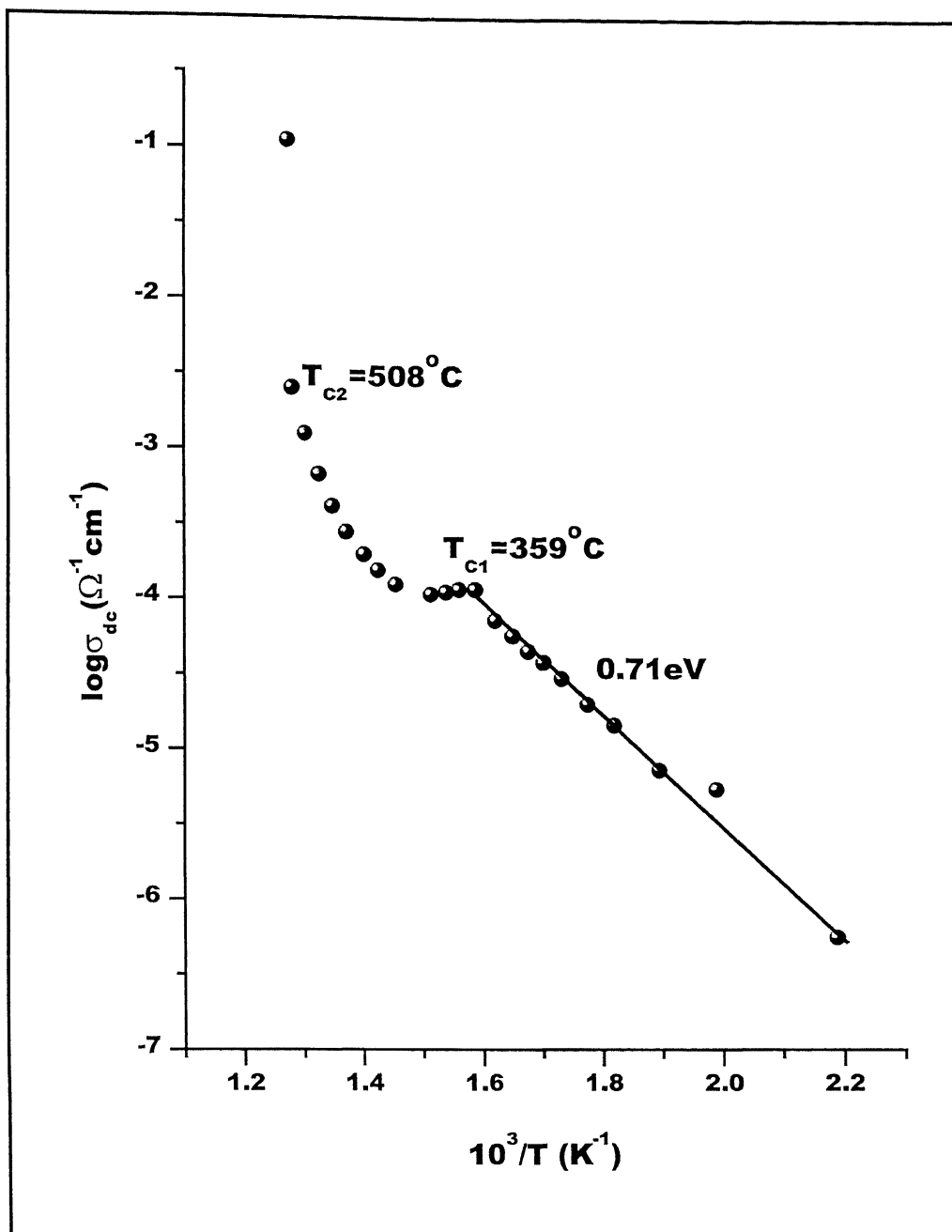


Fig.3.17: DC conductivity of $\text{Li}_2\text{SO}_4 + 80 \text{ m/o FeSO}_4$

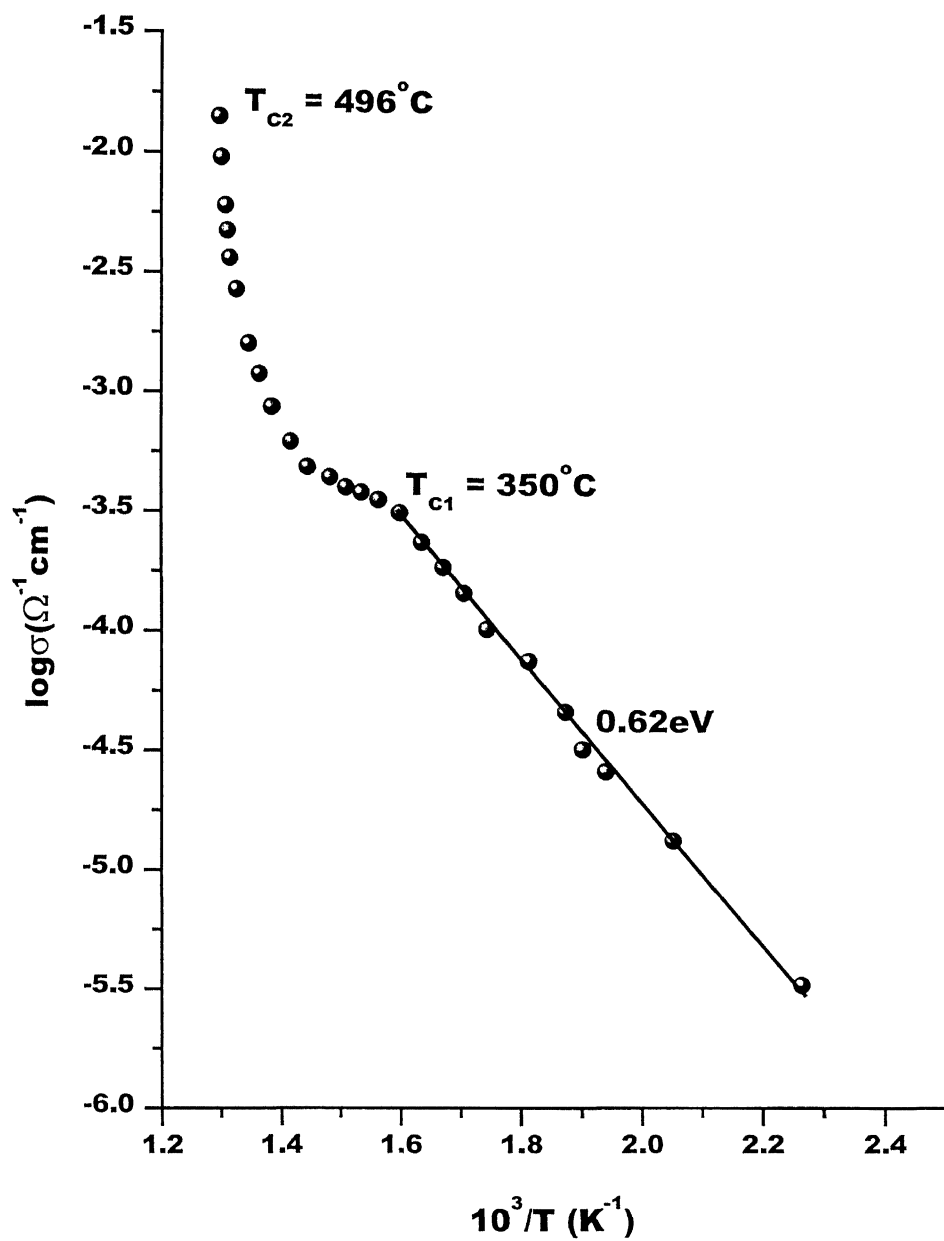


Fig.3.18: DC conductivity of pure FeSO_4

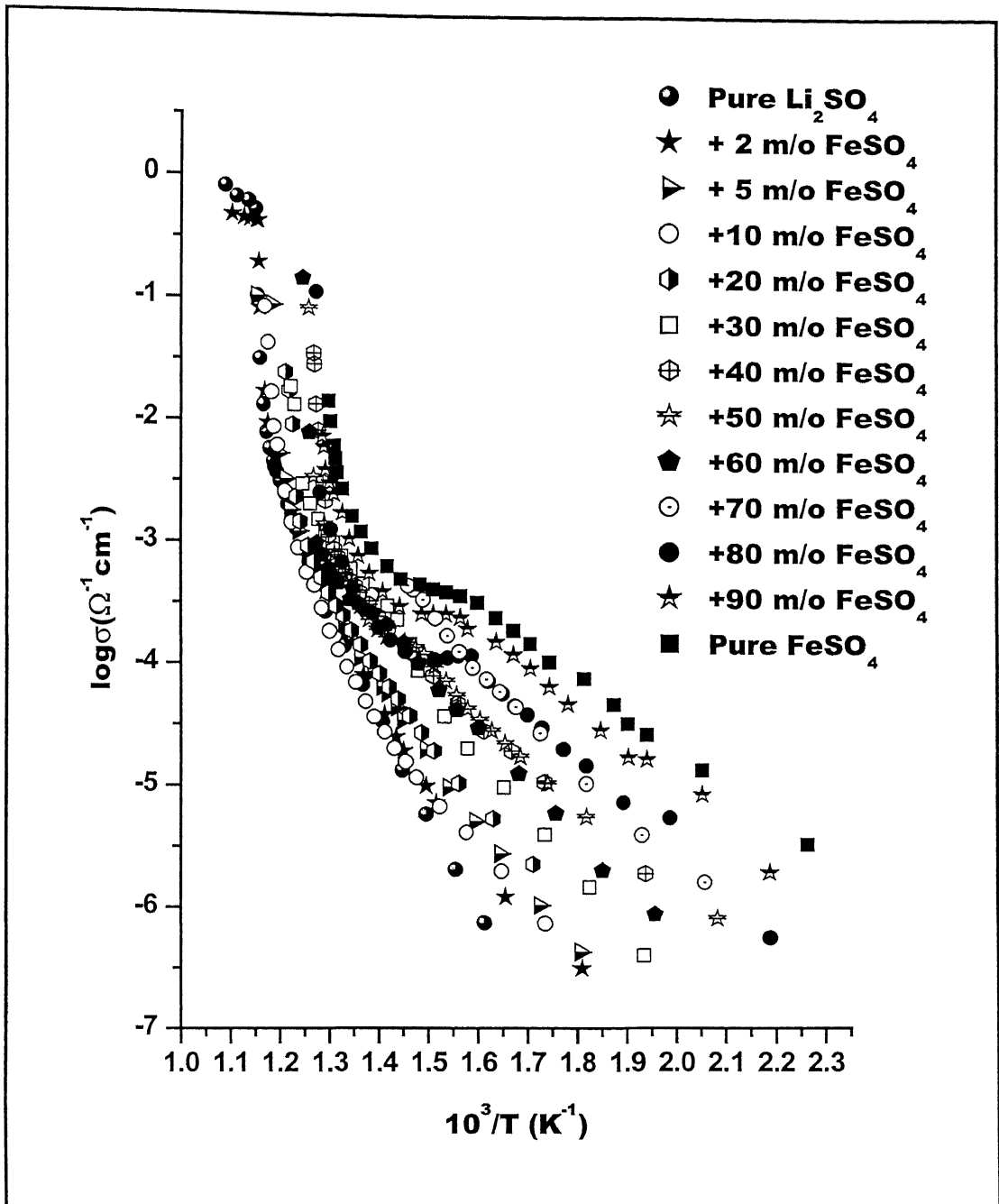


Fig.3.19: DC conductivities of all samples prepared by mechanical mixing

It is seen from the Figs.3.11-3.21 that the addition of 5 mol% FeSO_4 to Li_2SO_4 decreases the transition temperature by 18°C . The transition temperature (T_C) for pure Li_2SO_4 in our result is 584°C , whereas a somewhat lower value ($T_C = 575^\circ\text{C}$) is reported earlier [48]. The minor discrepancy in T_C is likely to be due to different impurity concentrations in the Li_2SO_4 samples and different heating rates rather than to errors in temperature measurements. It is experimentally found that different heating rates lead to different T_C 's but the activation energy required for various transitions remains the same. The decrease in T_C may be due to the fact that (i) the small Li^+ ion is replaced by bigger Fe^{2+} ions leading to lattice loosening and (ii) in order to maintain charge neutrality condition, more defects are produced. The concentration of defects increases on both counts. This results in enhancement in defect density and conductivity and hence lowering of the transition temperature, as a result of critical number of defects required to drive the β to α transition, as explained by Shahi *et al.* [49] for AgI system. Once the number of defects exceeds the critical concentration as required by a particular system for the phase transition, it undergoes the change, in order to minimize the Gibb's free energy, as required by thermal equilibrium. As the mole fraction of FeSO_4 increases the more number of defects are produced and it exceeds the critical value at still lower temperatures. The net result is a continuous decrease in transition temperature; in this case it is by 84°C by 40m/o FeSO_4 . It may be pointed out here though that the rate of lowering of T_C is too low in comparison to doped-AgI system [49].

The conductivity-temperature behaviour of Li_2SO_4 containing higher mole fractions of FeSO_4 is found to be nonlinear. Fig. 3.15 shows the result for 40 mol% FeSO_4 sample. This may be due to the fact that the ratio of the

fraction of two solid solution phases ss, namely Li_2SO_4 ss and FeSO_4 ss, is always changing with temperature, thus different activation energies are involved. For all the FeSO_4 -rich composites the activation energy in the low temperature region is 0.64-0.74 eV which is very close to that of pure FeSO_4 i.e. 0.62 eV. Therefore above 40 mol% FeSO_4 conductivity is purely determined by the FeSO_4 . This increase in the conductivity above 40 mol% is explained by the decrease in melting point observed in these cases, which is noted as T_{C2} . This decrease in melting point softens the lattice and hence there is a possibility of a structural change, which results in enhancement in the conductivity.

It has been widely shown that due to its high electronic polarizability, silver cations always exhibit conductivities in glass, which is 1 to 4 orders of magnitude higher than those exhibited by alkali ions [50, 51].

In general, atoms with a large ionic radius (e. g. high atomic number) exhibit more electron dipole response to an external electric field, because there are more electrons to respond to the field (electron screening effects also play a role in this response). This electronic contribution tends to increase the permittivity and hence polarization also [52].

As a result cation in FeSO_4 is more mobile than cation in Li_2SO_4 , since Fe^{2+} has higher atomic number than Li^+ . Hence FeSO_4 is more ionically conducting than Li_2SO_4 , in conformity with experimental results.

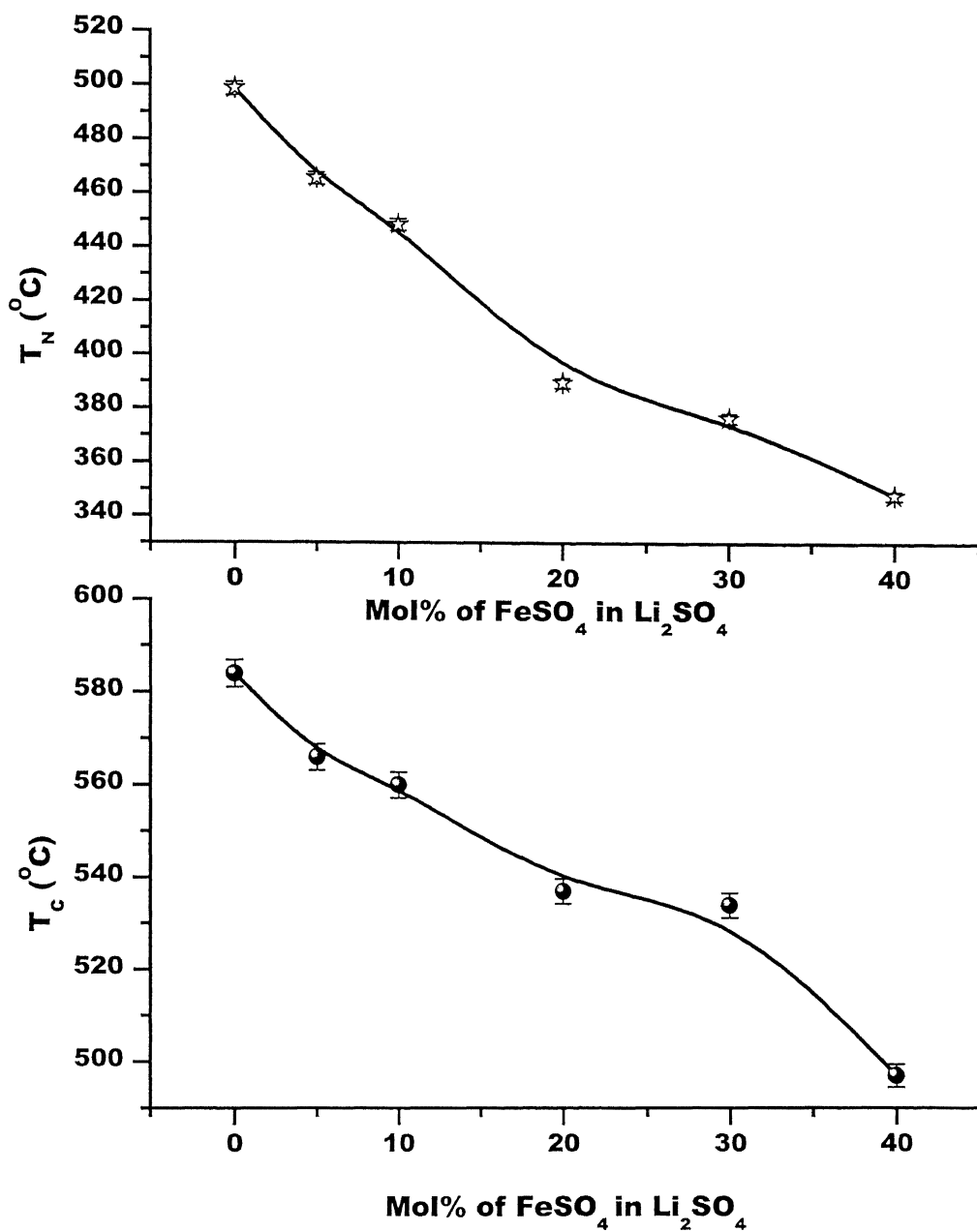


Fig.3.20: Plot of transition temperature (T_C) and knee temperature (T_N) against mole percentage of FeSO_4 in Li_2SO_4

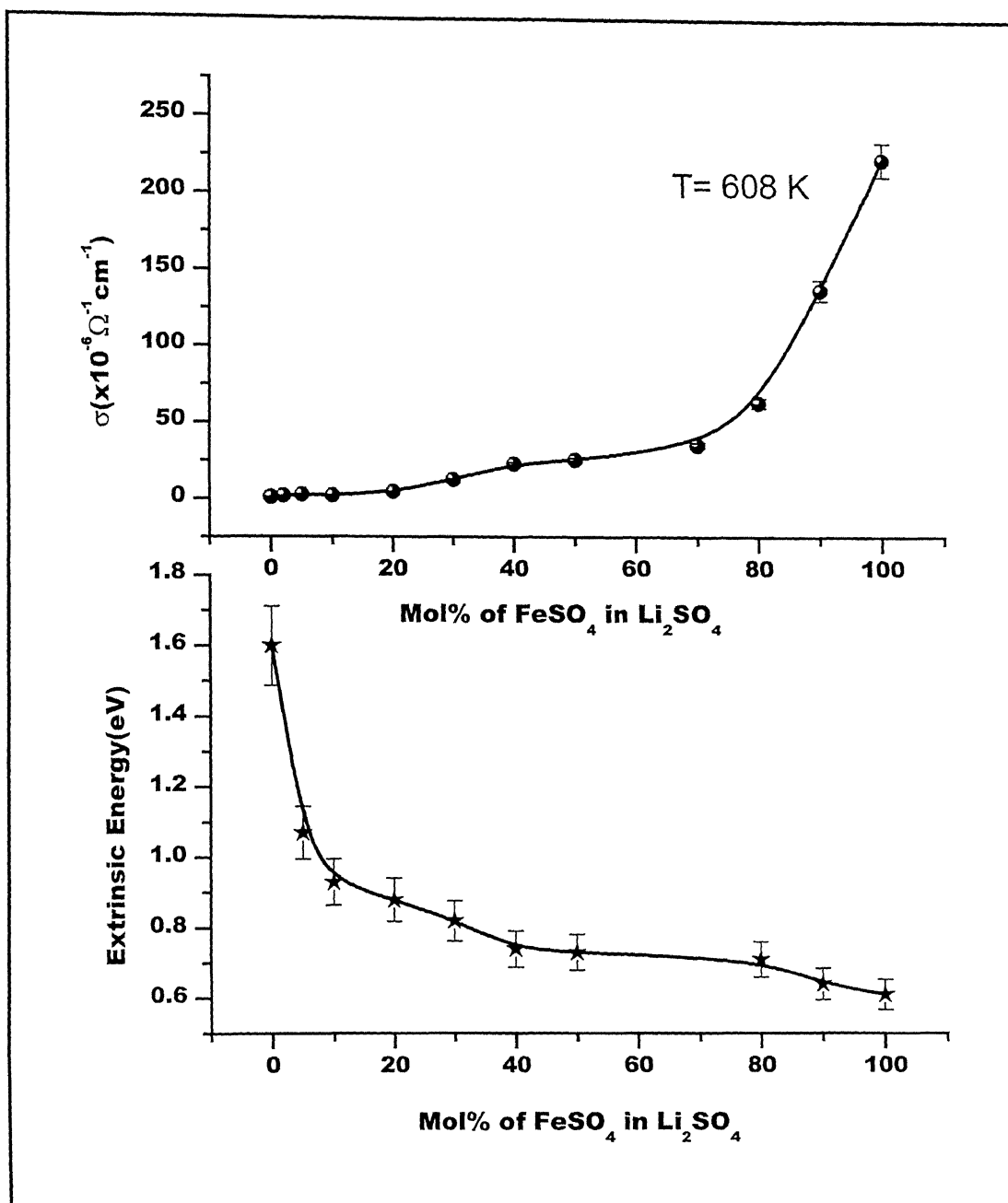


Fig.3.21: DC conductivity (σ) and extrinsic energy against mole percentage of FeSO_4 in Li_2SO_4

3.6 Maxwell Classical Model

From XRD results it is obvious that $\text{Li}_2\text{SO}_4\text{-FeSO}_4$ binary system is a two-phase composite system over the entire intermediate composition range. Therefore one can apply the Maxwell's rule of mixtures to explain the electrical conductivity results. According to the Maxwell model for composites, the conductivity of a composite electrolyte consisting of two constituents is given by

$$\sigma_{\text{composite}} = f_1\sigma_1 + f_2\sigma_2$$

where f_1 and f_2 are the mole fractions and σ_1 and σ_2 are the conductivities of the two constituents. The electrical conductivities are calculated using the above equation at 608 K. These along with the experimental values are given in Table 3.7. The following values of the conductivities of the two components (Li_2SO_4 and FeSO_4) are used in the above calculation.

$$\sigma_{\text{Li}_2\text{SO}_4} = 1.01 \times 10^{-6} \text{ ohm}^{-1} \text{ cm}^{-1} \text{ at } 608 \text{ K}$$

$$\sigma_{\text{FeSO}_4} = 233 \times 10^{-6} \text{ ohm}^{-1} \text{ cm}^{-1} \text{ at } 608 \text{ K}$$

Table 3.7: Experimental and calculated values of conductivities of $\text{Li}_2\text{SO}_4 + x \text{FeSO}_4$ system at 608 K

Composition (x) (Mole percentage)	Experimental σ_{dc} ($\text{ohm}^{-1}\text{cm}^{-1}$) $\times 10^{-6}$	Calculated σ_{dc} using Maxwell model($\text{ohm}^{-1}\text{cm}^{-1}$) $\times 10^{-6}$
0	1.01	-----
2	1.71	5.65
5	2.61	12.6
10	2.15	24.2
20	4.59	47.4
30	12.5	70.6
40	22.9	93.9
50	25.6	117
60	18.2	140
70	35.3	163
80	63.2	187
90	137	210
100	223	-----

It is noted immediately that the agreement between the observed and calculated conductivity values is not very good. More careful experiments may be carried out under controlled atmosphere to check these results.

CHAPTER 4

Summary and Conclusions

Samples of thirteen different compositions of $\text{Li}_2\text{SO}_4 + x\text{FeSO}_4$, with $0 \leq x \leq 1$ were prepared by two different techniques, viz., mechanical mixing and melting and quenching. Of these, mechanical mixing was found to be more effective. The different techniques that were used to characterize the mechanically-mixed samples include XRD, BET, FT-IR and impedance analysis.

The XRD patterns of $\text{Li}_2\text{SO}_4 + x \text{FeSO}_4$ showed that only $x \leq 0.10$ and $x \geq 0.70$ forming either complete or partial solid solutions and for $0.10 < x < 0.70$ it is a two-phase mixture at room temperature. In all the XRD patterns either characteristic peaks of FeSO_4 or that of Li_2SO_4 or both were present which indicates that there is no precipitation or intermediate phase. The particle size was analyzed using Peak Fit v(4) software for $\text{Li}_2\text{SO}_4 + x \text{FeSO}_4$, with $x = 0.0$ and 0.10 and was found to be ~ 13 and 60 nms respectively.

Four samples of $\text{Li}_2\text{SO}_4 + x \text{FeSO}_4$, viz. $x = 0.00, 0.20, 0.30$ and 0.40 were analyzed by FT-IR. The shift in vibrational frequencies may be due to the lattice distortion in SO_4^{2-} environment by the introduction of Fe^{2+} and modified peaks indicate a change in S-O distance.

BET measurements were done on samples $\text{Li}_2\text{SO}_4 + x \text{FeSO}_4$, with $x = 0.20$ and 0.30 and the specific area measured were 2 and $3.4 \text{ m}^2/\text{g}$ respectively. These low values of specific area indicate the surface contact may be poor which may affect the ionic conductivity.

The impedance analysis was done to measure the dc conductivity of the samples as a function of temperature. Then experiments were carried out for all the samples. Of these $\text{Li}_2\text{SO}_4 + x \text{FeSO}_4$, with $x \leq 0.4$, dc conductivity plot with inverse temperature showed two slopes with activation energy varying from 2.29-0.74 eV. The transition temperature reduced from 584°C for pure Li_2SO_4 to 497°C for 40 mol% FeSO_4 . For $\text{Li}_2\text{SO}_4 + 0.40 \text{FeSO}_4$ sample, the $\log \sigma$ vs. $1/T$ plot shows linear behavior and for $x \geq 0.40$ of $\text{Li}_2\text{SO}_4 + x \text{FeSO}_4$ it shows non-linear behaviour. The non-linearity may be due to the fact that the ratio of the mole fractions of two solid solution phases is changing with temperature, thus different activation energies are involved. Maxwell model of composites was not found to be satisfactory for $\text{Li}_2\text{SO}_4 + x \text{FeSO}_4$ two phase mixture.

There is evidence that the ionic-superionic (β - α) transition in Li_2SO_4 may also be driven by a critical concentration of defects as in case of AgI.

REFERENCES

- 1) M. Faraday "*Experimental investigations in electricity*", Quartich, London; **1340** (1839).
- 2) T. Takahashi, "*Materials for solid state batteries*," ed.by B.V.R. Chowdari and S. Radhakrishna, World Sci. Publ. Co., Singapore (1986).
- 3) P. W. M. Jacobs and F. C. Tompkins, *Q. Rev. Chem. Soc.*, **6**, 238 (1952).
- 4) C. Suresh, "*Superionic Solids*," North-Holland Publ. Co., 1981, p. 20.
- 5) M. O'Keefe and B. G. Hyde, *Phil. Mag.* **33**, 219 (1976).
- 6) T.Takahashi, *J. Appl. Electrochem.*, **3**, 79 (1973).
- 7) A. R. West, *J. Appl. Electrochem.*, **3**, 327 (1973).
- 8) C. E. Derrington, A. Lindner, and M. O'Keefe, *J. Solid State Chem.*, **15**, 171 (1975).
- 9) C. E. Derrington and M. O'Keefe, *Solid State Commun.* **15**, 1175 (1974).
- 10) L. E. Nagel and M. O'Keefe, "*Fast Ion Transport in Solids*," ed. Van Gool W., North Holland, Amsterdam, 165 (1973).
- 11) L. D. Landau and Lifschitz, "*Statistical Physics*," 2nd ed. Pergamon Press, New York (1968).
- 12) C. Sujata, *PhD thesis*, Kanpur, India (1992).
- 13) A. Benrath and K. Dreikopf, *Z. Phys. Chem.*, **99**, 57 (1921).
- 14) T. Forland and Krogh-Moe, *J. Acta. Chem. Scand.*, **11**, 565 (1957).
- 15) A. Kvist and A. Lunden, *Z. Naturforschg.* **20a.**, 235 (1965).
- 16) H.A. Oye, *Acta. Chem. Scand.* **18**, 361 (1964).
- 17) B. Jansson and C. A. Sjoblom, *Proceedings of the VIIth International Cong. Rheology*, 1976, p. 332.

- 18) H. Ljungmark, *Thesis*, Gothenberg, Sweden, 1974.
- 19) B. E. Mellander and L. Nilsson, *Z. Naturforsch.*, **38a**, 1396 (1983).
- 20) K. Schroeder and C. A. Sjoblom, *High Temp. High Press.*, **12**, 327 (1980).
- 21) C. A. Sjoblom, *Proc. 16th Inter Soc. Energy Conv. Engg. Conf.*, **1**, 958 (1981).
- 22) G. Meng, S. Tao and D. Peng, *Solid State Ionics*, **136**, 495(2000).
- 23) B. Zhu and S. Taob, *Solid State Ionics*, **127**, 83(2000).
- 24) M. Ganguli, M. H. Bhat and K. J. Rao, *Solid State Ionics*, **122**, 23(1999).
- 25) A. A. A. El-Rahmana, M.M. El-Desokyb and A. E. A. El-Sharkawyc, *J. Phys. Chem. Solids*, **60**, 119(1999).
- 26) B. M. Suleiman, M. Gustavsson, E. Karawacki and A. Lunden, *J. Phys. D.*, **30**, 2553(1997).
- 27) Y. Yan, W. Ruiling, M. Xucum and S. Pengshang, *J. Thermal Analysis*, **45**, 117(1995).
- 28) P. P. Fedorov, *Solid State Ionics*, **84**, 113(1996).
- 29) N. F. Uvarov, B. B. Bokhonov, V. P. Isupov, and E. F. Hairetdinov, *Solid State Ionics*, **74**, 15(1994).
- 30) N. H. Andersen, P. W. S. K. Bandaranayake, M. A. Careem, M. A. K. I. Dissanayake, C. N. Wijayasekara, R. Kaber, A. Lunden, B. E. Mellander, L. Nilsson and J. O. Thomas, *Solid State Ionics*, **57**, 203(1992).
- 31) K. Shahi and J. B. Jr. Wagner, *J. Phys. Chem. Solids*, **43**, 713 (1982a).
- 32) P. Manoravi and K. Shahi, *Solid State Ionics*, **45**, 83 (1991a).
- 33) P. Manoravi and K. Shahi, *J. Phys. Chem.*, **52**, 527 (1991b).

- 34) E. S. Barr (ed.), "*Infrared Physics*", Vol.1, 1(1961).
- 35) J. R. Macdonald (ed.), "*Impedance Spectroscopy*", John Wiley & Sons, Vol.1, 2 (1987).
- 36) W. I. Archer and R. D. Armstrong, *Electrochemistry*, **7**, 157(1980).
- 37) A. Hooper, *J. Phys. D.*, **10**, 1487(1977).
- 38) I. D. Raistrick, *Solid State Ionics*, **18/19**, 40(1986).
- 39) J. R. McDonald, *Solid State Ionics*, **13**, 147(1984).
- 40) B. D. Cullity(ed.), "*Elements of X-ray diffraction*", Addison-Wesley, 99(1959).
- 41) K. Shahi, *Phys.Stat. Solidi.*, **A41**, 11(1977).
- 42) K. Singh, *Solid State Ionics*, **66**, 5(1993).
- 43) K. Singh, V. R. Chandrayan and V. K. Deshpande, *Solid State Ionics*, **27**, 57(1988).
- 44) B. E. Mellander, D. Lazarus, *Phys. Rev.*, **B31**, 6801(1985).
- 45) A. Kvist, V. Trolle, *Z. Natureforsch.*, **A22**, 213(1967).
- 46) J. K. Aboagye and R. J. Friauf, *Phys. Rev.*, **B11**, 1654(1975).
- 47) B. E. Mellander, *Phys. Rev.*, **B36**, 5886(1982).
- 48) R. Aronsson, B. Heed, B. Jonsson, A. Lunden, L. Nilson, K. Schroeder and C. A. Sjöblom, "*Fast ion transport in solids*", North Holland, Elsevier (1979), pp.471-474.
- 49) K. Shahi, W. Weppner and A. Rabenau, *Phys. Stat. Sol.(a)*, **93**, 171(1986).
- 50) S. W. Martin, *J. Am. Soc.*, **74**, 1767(1991).
- 51) J. Kines and S. W. Martin, *Phys. Rev. Letters*, **76**, 70(1996).
- 52) G. D. Wilk, R. M. Wallace and J. M. Anthony, *J. Appl. Phys.*, **89**, 5267(2001).